Journal of Materials Chemistry A

REVIEW

View Article Online
View Journal | View Issue

Cite this: J. Mater. Chem. A, 2021, 9, 19410

Understanding the enhanced catalytic activity of high entropy alloys: from theory to experiment

Bing Wang, *[a] Yingfang Yao, [bc] Xiwen Yu,[b] Cheng Wang,[b] Congping Wu*[ac] and Zhigang Zou[abc]

High-entropy alloys (HEAs) have evolved to be one of the most popular materials in the last decade. Their unique configuration and attractive properties make HEAs one of the most promising catalysts. Although a very limited amount of work has been reported, higher activities of HEAs than traditional catalysts have been confirmed. This review firstly summarizes the current synthetic methods of nanostructured HEA catalysts. Then, four core effects of HEAs, namely high entropy, cocktail effect, lattice distortion and sluggish diffusion, are briefly introduced, and their impacts on the catalytic properties of HEAs are highlighted. The research progress in the application of HEAs in heterogeneous catalysis is subsequently reviewed from the perspectives of both theory and experiment. The relationships among metastable microstructures, substitution effects (*i.e.* strain, ligand and ensemble effects) and d-band center are discussed in detail, and their impacts on the adsorption energy of intermediates in catalytic reactions are emphasized. We conclude the review with the discussion of the challenges and opportunities of HEA catalysts. Several directions of future HEA research are put forward. The review provides a valuable resource for those interested in these exciting catalytic materials.

Received 1st April 2021
Accepted 24th June 2021

DOI: 10.1039/d1ta02718b

rsc.li/materials-a

1. Introduction

The synthesis and application (*e.g.* catalysis[1] and energy storage[2]) of high entropy alloys (HEAs) have received considerable attention in the recent years because of their promising properties that exceed the capabilities of a single element (or unary) component. HEAs are defined as alloys containing at least five principal metal atoms in equi-atomic or near equi-atomic ratios (each with concentrations between 5 at% and 35 at%).[3] Instead of forming intermetallic phases, HEAs favor the formation of single solid solution states with simple crystalline phases, namely face-centered cubic (FCC), body-centered cubic (BCC) or close-packed hexagonal (HCP) structure.[4] The thermal energy in the solid solution state of HEAs is sufficiently high to allow each element to have random positions within the structure.[5] An amorphous phase can also form if large atom size difference in HEAs causes severe lattice distortion.[6] Specific structures with appropriate compositions offer HEAs superior physicochemical properties to the traditional alloys, such as low-level stacking fault energy, thermal stability, radiation resistance and corrosion resistance.[7–15]

A promising area of research concerns the role of HEAs as heterogeneous catalysts in chemical and electrochemical reactions. The catalytic reactions are expected to be controlled by tuning the composition, surface atomic coordination and electronic configuration of HEAs. These microstructures can directly affect the interaction between intermediate species and catalysts, thus determining the catalytic activity and selectivity.

[a]Eco-materials and Renewable Energy Research Center (ERERC), School of Physics, Nanjing University, No. 22 Hankou Road, Nanjing 210093, P. R. China. E-mail: bingwang@nju.edu.cn

[b]College of Engineering and Applied Sciences, Nanjing University, No. 22 Hankou Road, Nanjing 210093, P. R. China

[c]Kunshan Innovation Institute of Nanjing University, 1699 Zuchongzhi South Road, Kunshan, Jiangsu 215347, P. R. China

Dr Bing Wang is an associate professor in the School of Physics at Nanjing University in Nanjing, China. She received her PhD from Nanjing University in 2014. She was successively an assistant professor at Nanjing University (China) and a postdoctoral research associate at Georgia Institute of Technology (USA). Her work has been focusing on the synthesis of novel and functional nanostructured materials, including semiconductors, high-entropy nanoparticles and metallic nanocrystals, for exploring their potential use in electrocatalysis, photocatalysis, photoelectrochemistry or solar cells.

Therefore, engineering the microstructures is a feasible and reasonable approach to make HEAs a promising catalyst with desirable functions. Although the field of HEAs began in 2004,[3,16] only in recent years has attention been paid to the catalytic application of HEAs.[17] Minimizing the HEA particle size to the micron or even nanometer scale is the key and challenge to the development of efficient HEA catalysts. In 2018, a thermal shock method was reported to alloy dissimilar elements into HEA nanoparticles (NPs), which greatly stimulated the blossom of HEAs in catalysis. A wide range of multicomponent nanoscale HEAs with the desired composition and size can be achieved by controlling the carbothermal shock parameters.[18]

Based on the results of the limited investigations performed so far, HEAs are expected to be emerging catalytic materials in the future. In this review, the advantages and potential of HEAs as catalysts are showcased based on the current theoretical calculation and experimental results. First, we summarize the current preparation methods of nanostructured HEA catalysts in Chapter 2. The drawbacks of the current synthesis methods are highlighted. Next, the core effects of HEAs (*i.e.* high entropy, cocktail effect, lattice distortion and sluggish diffusion), which play crucial roles in improving the catalytic performance, are emphasized in Chapter 3. Some unique properties of HEAs resulting from the core effects are then introduced in Chapter 4, including metastable microstructures, substitution effects (*i.e.* strain, ligand and ensemble effects), d band center and adsorption energy. How these effects modify the d-band is emphasized. In particular, we discuss the mechanisms behind the remarkable catalytic activity and stability induced by these properties. Challenges associated with HEA catalysts are finally clarified, and several perspectives for future research directions and development of HEAs in the field of catalysis are suggested in Chapter 5. This work aims to be a comprehensive and critical review of general interest to communities who focus on efficient catalysts. It can provide guidance for synthesizing high-quality HEA nanoparticles with improved catalytic performance.

2. Synthesis strategies of nanostructured HEAs

Synthesis of HEA catalysts with nanostructures is the foundation for their application in heterogeneous catalysis. The controlled combination of multiple metals in HEAs at the nanoscale provides an effective avenue to tune the properties by maximizing the active surface area-to-volume ratio. Different from their bulk materials, HEA nanostructures possess unique size-dependent optical and electronic properties, followed by their unique chemical properties, which contribute to achieving highly efficient performance in catalysis. The controllable incorporation of multiple immiscible elements into one type of nanoparticle merits untold scientific and technological potential, yet remains a challenge using conventional synthetic strategies. Very recently, some facile and straightforward strategies for the synthesis of HEA nanomaterials have been developed, which shed light on the application of HEAs in catalysis. Moreover, the drawbacks of each strategy, which should be overcome in further research, are also pointed out.

2.1 Carbothermal method

Hu *et al.* used a two-step carbothermal-shock method to alloy up to eight elements into HEA NPs (NPs),[18] which makes it an important advance in promoting the development of HEAs (Fig. 1). This strategy involves a 55 millisecond flash heating and cooling of metal precursors on carbon supports at a peak temperature of 2000 K in argon. The high temperature ensures uniform mixtures of multiple elements by fission/fusion mechanisms and catalytically driven particle dispersion mechanism. During the synthesis process, the liquid metal splits to harvest the dispersed surface-bound residual oxygen (O*) on the carbon support. The concentration of O* closely relates to the density of defects on the support. The presence of O* and the use of catalytically active metals allow different compositions into single particles during the carbothermal process. Notably, a higher O* concentration drives more frequent catalyst motion, making the NPs coarser, whereas a lower concentration may result in a decreased mobility, preventing the formation of single NPs.

Although the carbothermal shock method can craft HEA NPs with controllable composition and ultrafine size, it only produces NPs immobilized on a carbon substrate due to the extreme synthetic conditions. It is incompatible with thermally sensitive substrates such as metal, glass, and polymers.

2.2 Electrosynthesis method

In contrast to thermal approaches, electrodeposition is a room-temperature strategy for the synthesis of amorphous metal NPs on conductive substrates.[19] Recently, Dick *et al.* used this method to fabricate high-entropy NPs with up to eight principal components by confining their salt precursors to water nanodroplets suspended in dichloroethane.[6] The formation of a ~10 nm nanodroplet/electrode contact radius leads to the electrodeposition of alloy NPs with disordered microstructures on highly oriented pyrolytic graphite (HOPG) or glassy carbon substrate electrodes.[6] The collision of the nanodroplet with the electrode induced an initial sharp rise of current response, followed by a decay due to the consumption of the salts inside the nanodroplets.[20] The electrodeposition takes *ca.* 100 ms to synthesize the HEA NPs with an average diameter of 900 nm.[6] The nanodroplet-mediated electrodeposition can prevent phase separation, allowing precise stoichiometric control with 2–5% variability.[6]

Despite many advantages, this method can only produce HEA NPs in the amorphous phase. In addition, it is difficult to achieve uniform immobilization of HEA NPs on granular supports.

2.3 Solvothermal-pyrolysis method

Huang *et al.* developed a solvothermal-pyrolysis approach to prepare HEA NPs.[21] As shown in Fig. 2, typically a nanorod-

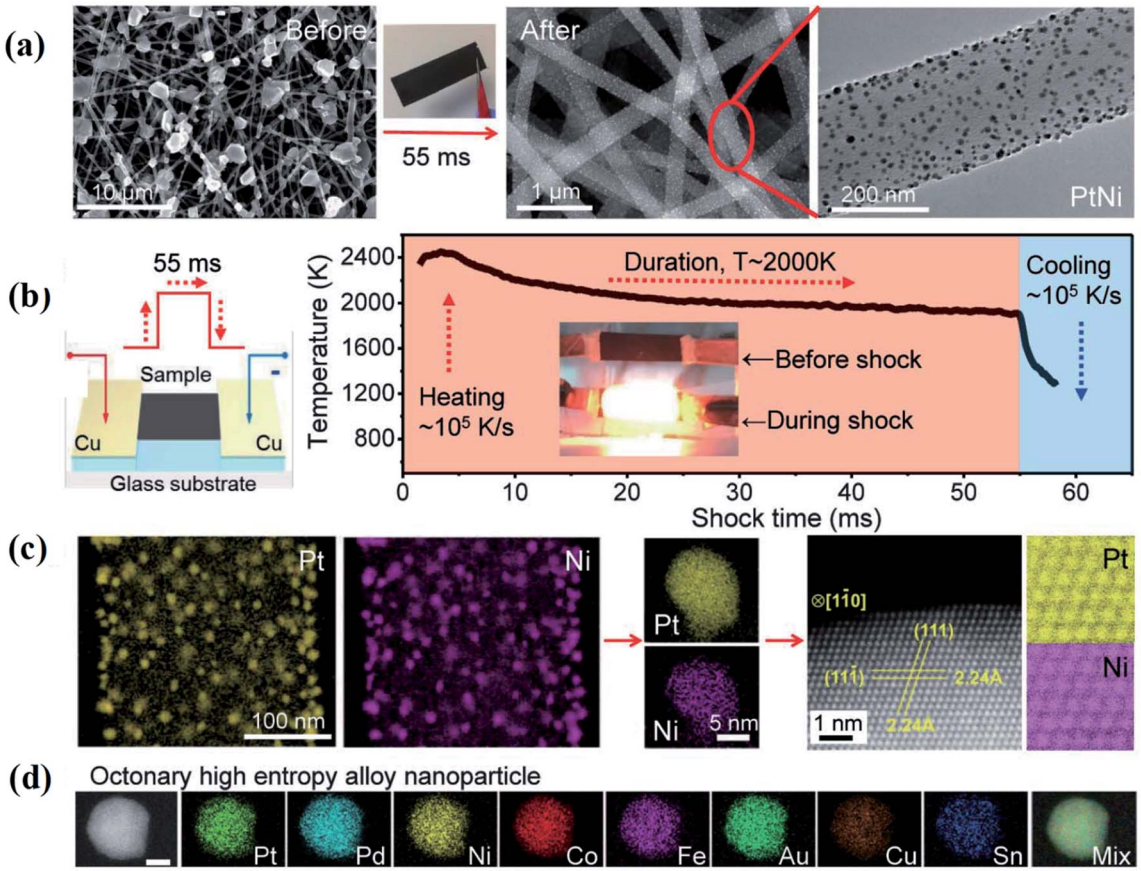

Fig. 1 Carbothermal shock synthesis of HEA NPs on carbon nanofiber (CNF). (a) SEM of metal precursors on CNF, and the synthesized PtNi NPs after the carbothermal shock method. (b) Sample preparation and the temporal evolution of temperature during carbothermal shock. (c) Low-magnification and single-particle elemental maps, an HAADF image, and corresponding atomic maps for a PtNi alloy. (d) Elemental maps of an HEA NP composed of Pt, Pd, Ni, Co, Fe, Au, Cu, and Sn. Scale bar, 10 nm. Reproduced from ref. 18 with permission from The American Association for the Advancement of Science.

shaped precursor of quinary metal–organic frameworks (MOFs) on the surface of carbon cloth (CC) was synthesized *via* a solvothermal method in the solution mixed with salt precursors and 2,5-dihydroxyterephthalic acid.[21] Then the precursor was treated by pyrolysis in a H_2/Ar mixed atmosphere, which induced decomposition of the MOFs to form single-phase FCC HEA NPs with a diameter of 5 nm.[21] The HEA NPs prepared by this method possess many partial dislocations and stacking faults as well as the displacement of atoms, indicating the high distortion of atomic lattices of the NPs. These defects in HEAs result in surface tension, which will significantly affect the catalytic performance. Notably, the pyrolysis process is conducted in a fixed bed pyrolysis reactor. The metal ions are prone to sequential reduction due to their different chemical reductive potentials, causing phase separation.[22]

Lu *et al.* developed a fast-moving bed pyrolysis (FEBP) strategy to synthesize HEA NPs on granular supports including carbon, γ-Al_2O_3 and zeolite (Fig. 3). This method was conducted at 923 K with a population speed of 20 cm s^{-1}, resulting in the formation of a small size (~2 nm) of HEA NPs within 5 s. The critical size of HEA nucleus is small enough to reduce excess free energy used for forming nanoalloys, thus avoiding phase separation.[23] It is demonstrated that when the time for the precursors to reach the heating zone increases from 5 s to 20 s, obvious phase separation has been found in NPs.[24] In the fast moving bed pyrolysis strategy, all metal precursors with different reduction potentials can be decomposed at 923 K.[24] The formation of HEA NPs without phase separation is thermodynamically favored because of the low critical free energy.[23] In contrast, a slow moving bed pyrolysis causes a larger radius of nuclei, and thus results in phase separation.[25]

Iversen *et al.* reported a solvothermal autoclave synthesis method to synthesize HEA NPs at 200 °C in an acetone–ethanol solution with metal precursors.[26] Metal chloride salts are prone to yielding the HCP phase, whereas the acetylacetonate precursors craft the FCC phase, due to their different pre-nucleation structures.[27] Homogeneous HEA NPs were generated at a temperature lower than the reduction temperature of the metals in HEAs due to autocatalyzed metal reduction at the (111) facets of the FCC phase.[28] A Pd core is initially formed which would autocatalyze the reduction of the other metals on the (111) facets. Growth along the [111] direction occurs in the initial 20 min, whereas the growth rate along the perpendicular direction is small, inducing elongation of the HEA NPs.[28] The

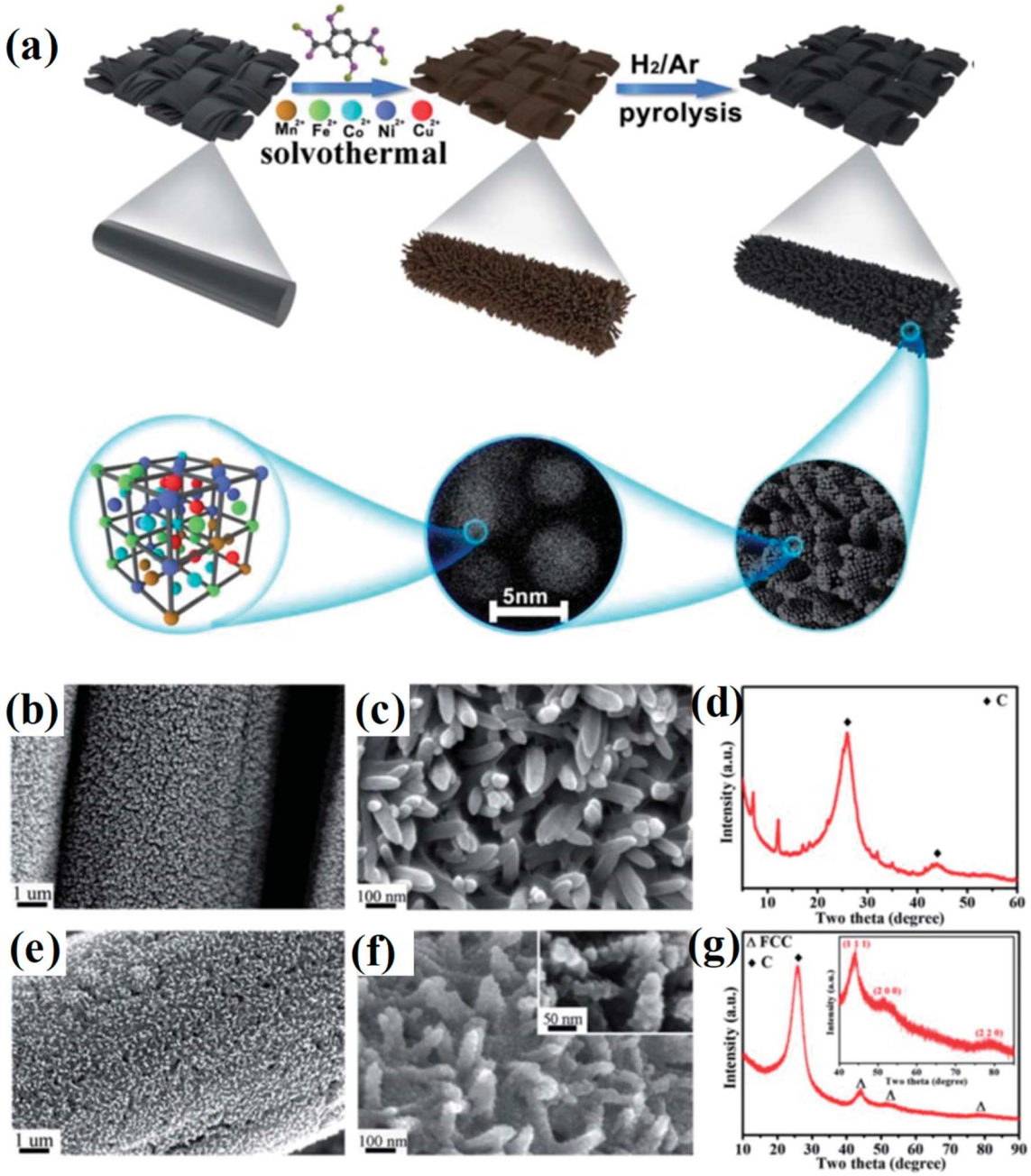

Fig. 2 (a) Schematic of the synthesis of HEA composites. (b and c) FESEM images, (d) XRD of quinary MOFs/CC, (e and f) FESEM images, and (g) XRD spectrum of HEA@ N-doped porous carbon on the surface of CC treated at 450 °C. Reproduced from ref. 21 with permission from the Royal Society of Chemistry.

alloying of HEAs by solvothermal reactions, governed by the reduction rates, is a kinetically driven process rather than thermodynamic energy gain of mixing.[28] However, products of solvothermal reactions are inevitably inhomogeneous comprising particles with agglomerated crystallites deviating from the main HEA phase.

2.4 Mechanical milling approach

Srivastava *et al.* first used a mechanical milling and sonication assisted exfoliation approach to synthesize HEA NPs of NiFeCrCoCu on graphene.[29] This method involves two steps: firstly, a multimetal-graphite composite was produced by mechanical milling of graphene rod and metal powders. Secondly, the composite was subjected to sonication for exfoliation to produce multi-metal HEA nanoparticle decorated graphene. The presence of metal powders within the interlayer spacing of graphene causes strain, and thus facilitates the exfoliation process during sonication to form HEA NPs. However, the HEA NPs synthesized by the mechanical milling method display a large distribution in the composition. As

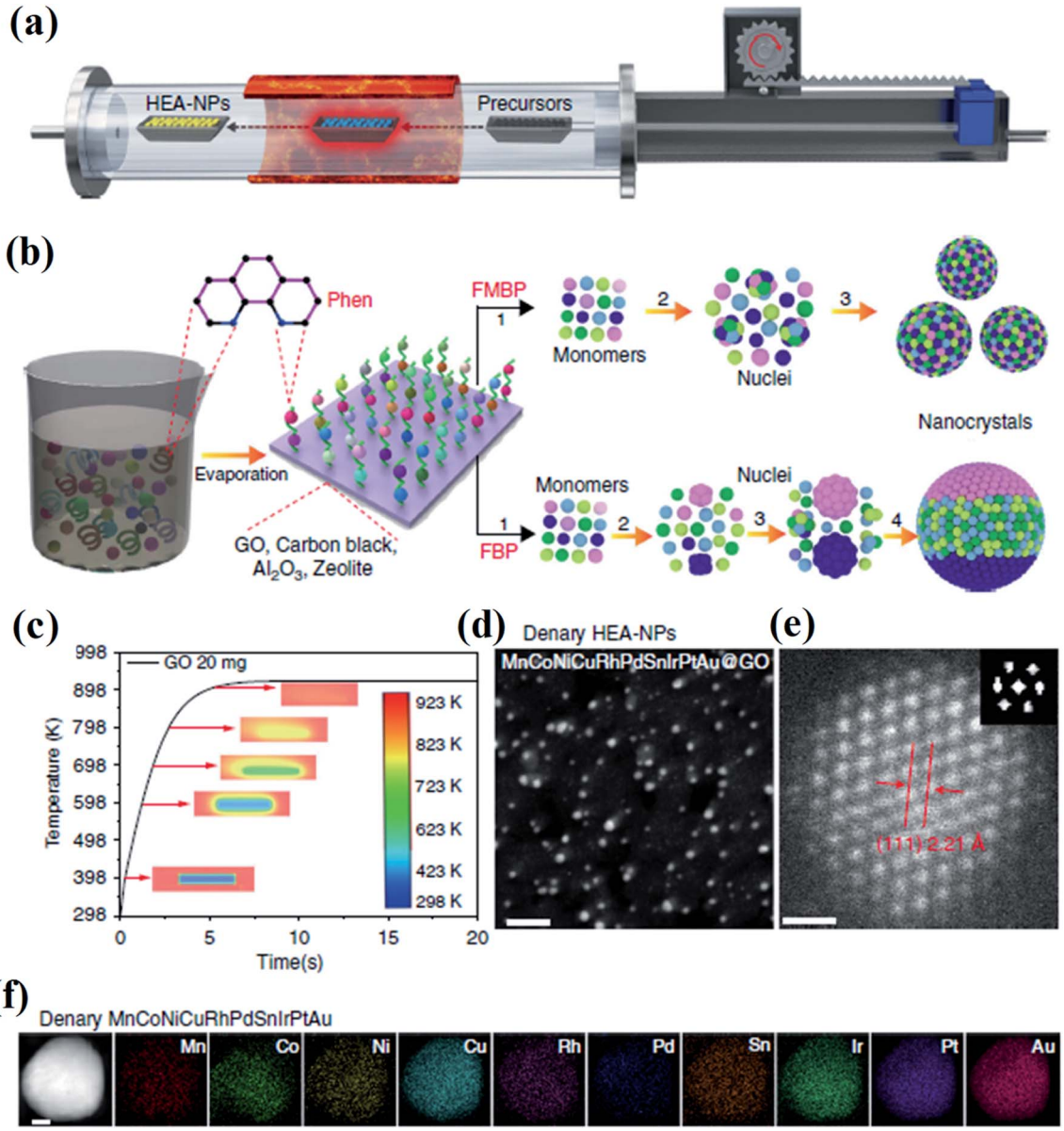

Fig. 3 (a) Schematic diagram of the FMBP setup for the synthesis of HEA NPs. (b) Schematic diagrams for the synthesis of homogeneous and phase-separated HEA NPs by FMBP and fast bed pyrolysis (FBP) strategies, respectively. (c) The simulation of the time required for precursors/GO to reach 923 K in the FMBP process. The images in the center show the metal precursors/GO in the quartz boat. (d) HAADF-STEM images for the denary (MnCoNiCuRhPdSnIrPtAu) HEA-NPs highly dispersed on GO synthesized by the FMBP strategy; scale bar, 10 nm. (e) The HRSTEM image for the denary (MnCoNiCuRhPdSnIrPtAu) HEA-NPs (inset: Fourier transform analysis for the denary (MnCoNiCuRhPdSnIrPtAu) HEA-NPs); scale bar, 0.5 nm. (f) Elemental maps for the denary (MnCoNiCuRhPdSnIrPtAu) HEA-NPs. Scale bar, 10 nm. Reproduced from ref. 24 with permission from Springer Nature.

shown in Fig. 4, the amount of Ni is the lowest among the five component elements in HEA NPs.

2.5 Wet chemical synthesis

Wet chemical synthesis, dealing with chemical reactions in solution, is one of the most frequently used routes to obtain high yields of nanostructured materials. This approach enables fine tuning of the reaction conditions, such as temperature, pressure, and pH, to achieve precise control over the morphology and compositions of NPs, and further their optical, electronic and surface properties. Alloy NPs can be crafted by wet chemical synthesis *via* co-reduction of metallic ions.[30,31] Recently, alloys with compositions of more than five elements have been successfully fabricated under ambient conditions *via* an ultrasonication-assisted wet chemistry method.[32] The ultrasonication can lead to the formation, expansion, and collapse of bubbles in liquid, resulting in a localized hotspot by the conversion of the kinetic energy of the liquid motion.[33,34] Under ultrasonication irradiation, Dai *et al.* successfully synthesized the HEA quinary NPs of

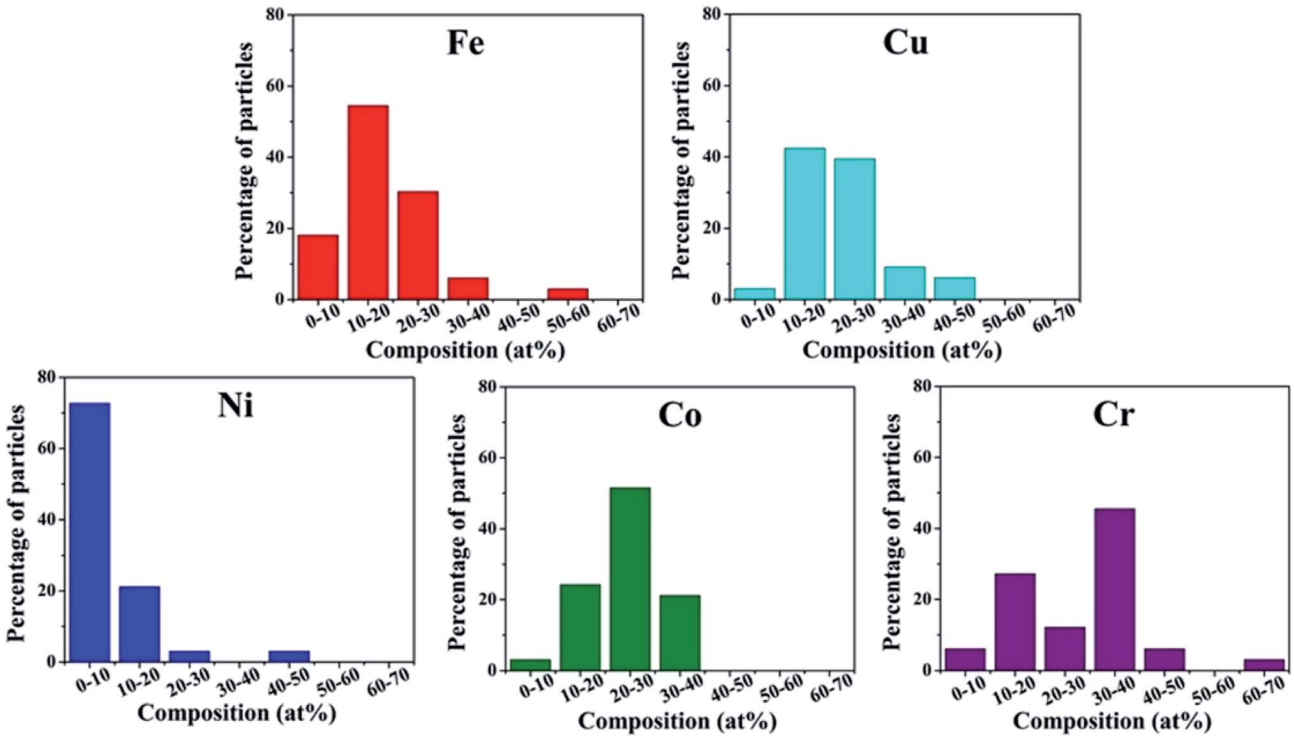

Fig. 4 Histogram distribution of Fe, Cu, Ni, Co, Cr elements in HEA NPs synthesized by the mechanical milling technique. Reproduced from ref. 29 with permission from Springer Nature.

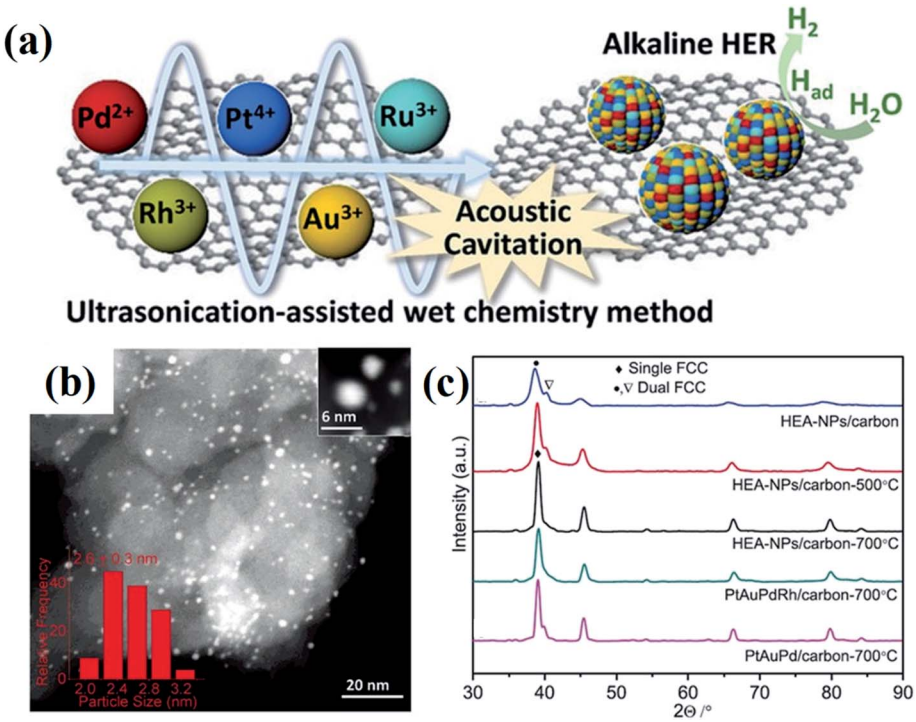

Fig. 5 (a) Schematic illustration of the synthesis of PtAuPdRhRu supported on XC-72 carbon and its application in HERs. (b) STEM image of PtAuPdRhRu/XC-72 carbon. (c) XRD patterns of PtAuPdRhRu/carbon synthesized by an ultrasonication-assisted wet chemistry method under different conditions. Reproduced from ref. 32 with permission from John Wiley and Sons.

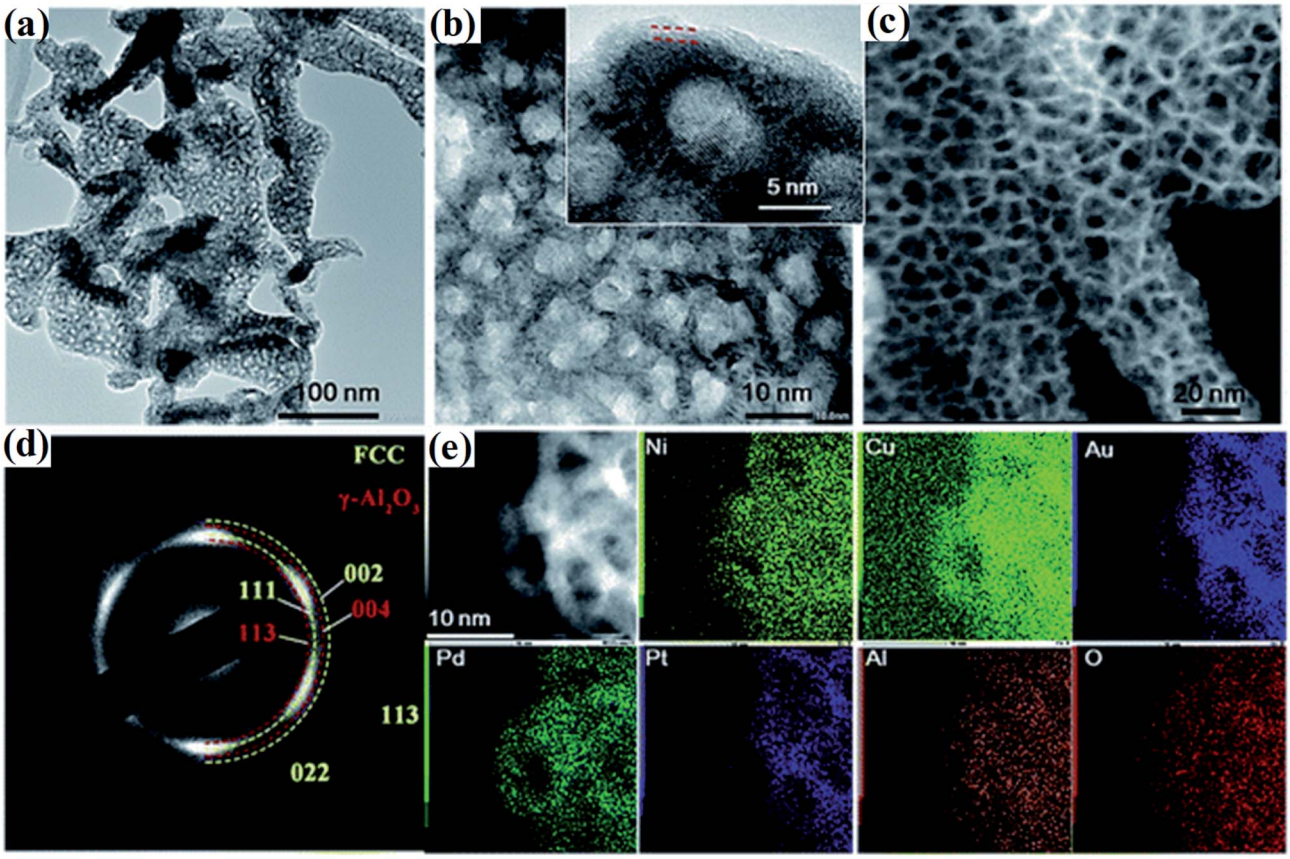

Fig. 6 (a and b) TEM images of the dealloyed senary AlNiCuPtPdAu at different magnifications. (c) Dark-field STEM image, (d) the corresponding SAED image and (e) STEM-EDS mapping of AlNiCuPtPdAu. The inset of (b) shows the lattice fringe of the ligaments and the formed thin oxide layer. Reproduced from ref. 38 with permission from the Royal Society of Chemistry.

PtAuPdRhRu with diameters of less than 3 nm by co-reduction of their corresponding cations at room temperature with ethylene glycol as both the reductant and solvent.[32] The HEA-NPs/carbon produced by the ultrasonication-assisted wet chemistry method displays a two-phase microstructure of FCC (Fig. 5).[32]

Notably, the synthesis of HEA NPs by the chemical reduction strategy is challenging, particularly, when the redox potentials

Table 1 Synthetic strategies of HEA NPs

Strategy	Driving force	Experimental conditions	Elements	Structure	Substrate applicability	Duration time	Elemental distribution	Ref.
Carbothermal shock	Electrically triggered Joule heating	2000 K, argon	Pt, Pd, Co, Ni, Fe, Au, Cu, Sn	FCC, NPs	Carbon substrates	55 ms	Good	18
Electrosynthesis	Electro-shock	RT, air	Pt, La, Co, Cr, Cu, Gd, In, Mn, Ni, V	Amorphous, NPs	Graphite	100 ms	Good	6
Moving bed pyrolysis	Pyrolysis	923 K, argon	Pt, Au, Ir, Sn, Pd, Rh, Cu, Ni, Co, Mn	FCC, NPs	Carbon, Al_2O_3, zeolite	5 s	Good	24
Solvothermal pyrolysis	Pyrolysis	700 K, argon	Mn, Fe, Co, Ni, Cu	FCC, NPs	Carbon cloth	>5 h	Poor	21
Mechanical milling	Mechanical force	RT, air	Ni, Cr, Co, Cu, Fe	FCC, NPs	Graphene	>80 h	Poor	29
Wet chemistry	Ultrasonication & reduction	973 K, nitrogen	Pt, Au, Pd, Rh, Ru	FCC, NPs	Carbon	>5 h	Poor	32
Liquid metal dealloying	Heat & chemical reaction	>873 K, argon	Al, Ni, Cu, Pt, Pd, Au, Co, Fe, Mo	FCC, nanoporous	W/O	>5 h	Poor	38
Reaction sputter deposition	Magnetron sputtering	5×10^{-6} torr	Pt, Fe, Co, Ni, Cu, Ag	FCC, NPs	Gas diffusion electrodes	>25 h	Poor	40
Pulsed laser ablation	Pulsed laser	RT, air	Co, Cr, Fe, Ni, Mn	FCC, NPs	W/O	~ms	Good	44

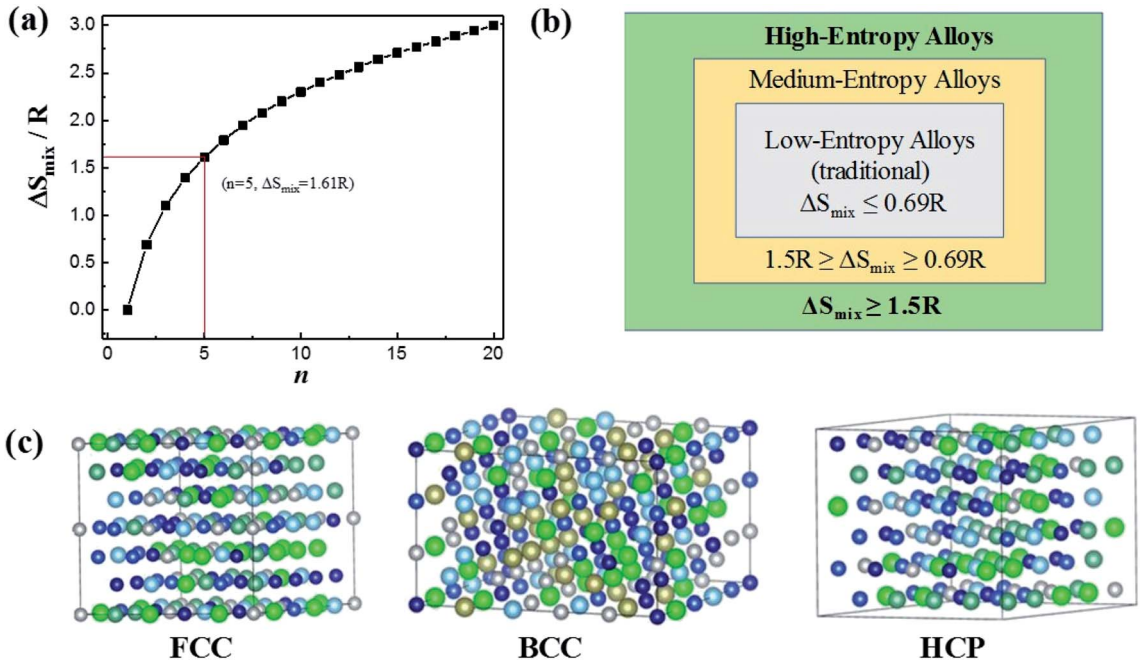

Fig. 7 (a) ΔS_{mix} as a function of the number of principal components for equimolar alloys. (b) Alloy definitions based on configurational entropy. (c) Structural illustration for the FCC, BCC and HCP phases of HEAs. Reproduced from ref. 51 with permission from Frontiers.

of individual components differ substantially. It is prone to yielding alloy NPs with severe phase separation.

2.6 Liquid metal dealloying

Liquid metal dealloying is a general and scalable strategy to prepare ultrafine nano-porous HEAs with enhanced surface areas and uniform pore structures.[35,36] In a typical process, HEA nano-structures are prepared by firstly melting pure metals in a furnace in an inert atmosphere. Then the liquid metal is spun to prepare the alloy ribbons, followed by chemical dealloying in an alkaline aqueous solution under sonication. Noble metals such as Ir, Pt, Au, Rh, and Ru are easily obtained by dealloying, whereas some transition metals such as Co, Fe, Ni, Cr, and Mn are prone to oxidation during dealloying.[37] Thus, the overall atomic ratio of the active transition metals should be low when using the dealloying strategy to prepare nano-porous HEAs.

It has been proven that nano-porous HEAs prepared by the dealloying technique (see Fig. 6) are stable under both annealing and electrochemical cycling conditions due to a thin conformal oxide coating.[38,39] Moreover, such a coating improves the catalytic activity of CO oxidation by increasing the efficiency of O_2 dissociation which is the rate-limiting step for CO oxidation. Nevertheless, the liquid metal dealloying process for the preparation of the precursor alloy is a high-cost technique due to the requirement of high temperature and an inert atmosphere.

2.7 Reactive sputter deposition

The reactive sputtering process is used to deposit crystalline multi-element film with controlled reactive magnetron sputter deposition. The technique is based on ion bombardment of the target material to generate vapor *via* a physical process. The deposition condition is critical to control the grain size, orientation and nanostructures of multi-element films. Therefore, it is feasible to employ the sputter deposition to create HEA NPs for catalytic studies.[40] Crafting $Pt_{50}Fe_{11}Co_{10}Ni_{11}Cu_{10}Ag_8$ HEA NPs on noncatalyzed gas diffusion electrodes by the sputter process has been reported.[40] Crystalline FCC phases were confirmed by XRD analysis, indicating that annealing treatment is not required to form the solid-solution phase of the HEA NPs. With a calculated deposition rate of 5.2 nm min^{-1}, the sputtering process leads to a distinct morphological evolution during the preparation of a thin layer of HEAs. Increase of the sputtering time coarsened the NPs with larger nodules on the surface. The $Pt_{50}Fe_{11}Co_{10}Ni_{11}Cu_{10}Ag_8$ demonstrated better catalytic ability and stability than the pure Pt in the catalytic reaction of methanol oxidation.[40]

A major drawback of reactive sputtering is its complexity. Some fundamental aspects of the process have not been elucidated yet, which makes it difficult to understand the properties of the obtained HEA NPs as a function of the deposition conditions.

2.8 Pulsed laser ablation

Pulsed laser ablation (PLA) from a solid target emerged as a "green" alternative physical route for a scalable nanofabrication.[41] A focused laser used in this technique can induce photothermal effect that rapidly generates a confined high-temperature field at a specific area. It has proven useful for making single nanoparticles[42] and even binary alloys.[43] Gokce *et al.* used the PLA method to synthesize CoCrFeNiMn HEA NPs by irradiating a picosecond pulsed laser on the surface of an

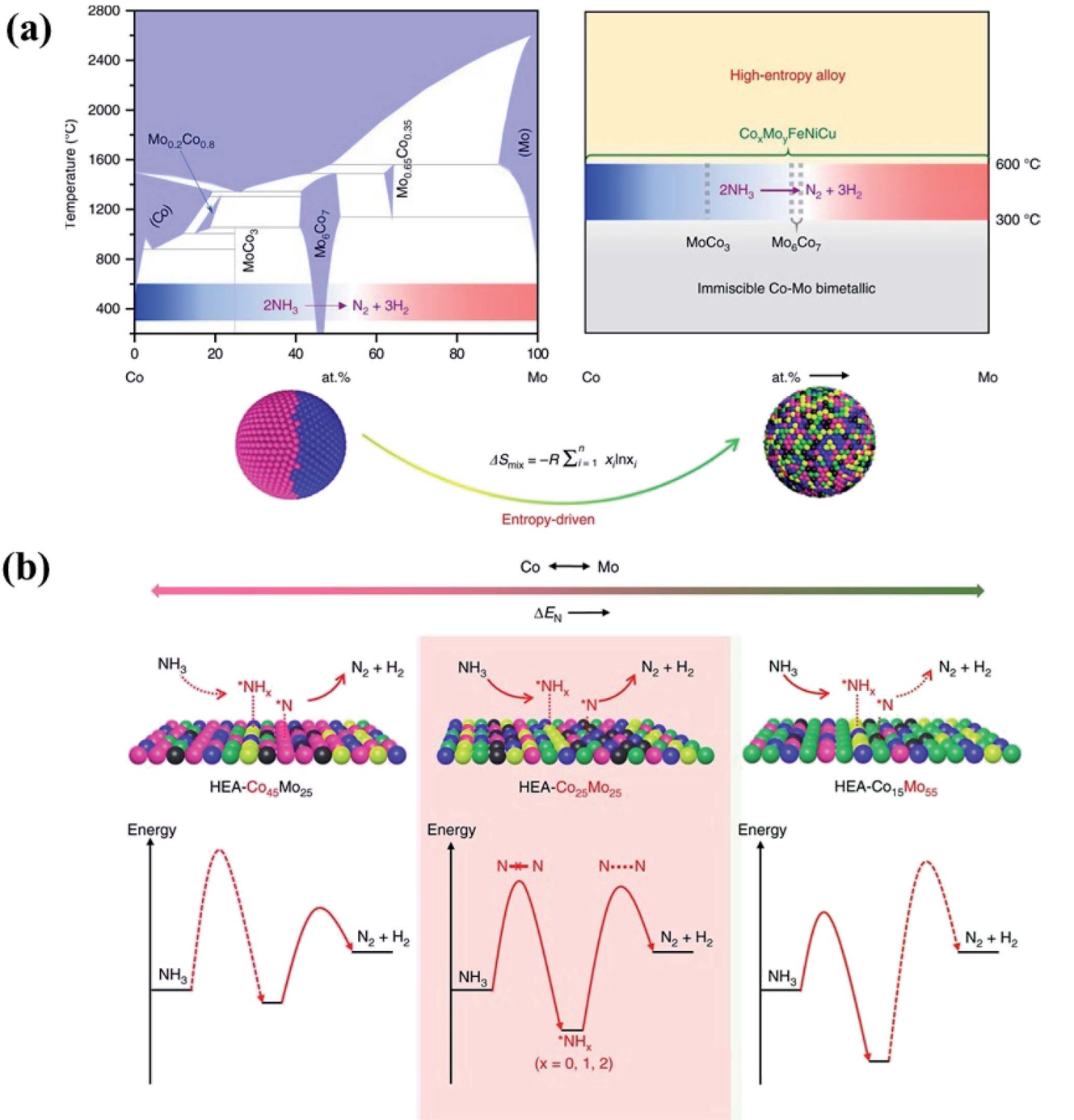

Fig. 8 (a) HEA catalysts preventing a large miscibility gap which presents in conventional binary alloys. (b) Schematic illustration of the rate-limiting factors in NH_3 decomposition, labeled with dash lines in the lower panel. On a Co-rich surface (left), the rate is limited by activation or dehydrogenation of NH_3; on a Mo-rich surface (right), the rate is limited by the recombinative desorption of *N; the balance for these two steps is reached on an intermediate composition with uniform distribution of Co and Mo atoms. Reproduced from ref. 56 with permission from Springer Nature.

original ablation target in ethanol solution.[44] Although this is an impressive demonstration of synthetic capabilities, corresponding targets are usually required to fabricate the NPs, which greatly limits the technique extension and application. Furthermore, the conventional "planar" geometry of the targets may slow down or stop the nanofabrication process since the laser intensity on the target surface would be gradually weakened with the continuous production of NPs in the system,[45] leading to uneven diameter distribution and uncontrolled growth of nanoclusters.

Based on the above discussion, we summarize each synthetic strategy in Table 1, including the driving force, experimental

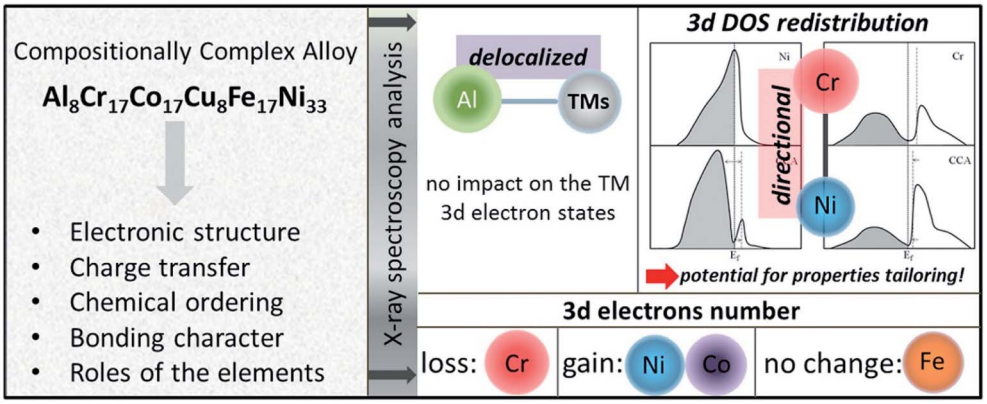

Fig. 9 The altered properties of HEAs as compared to the corresponding pure metals. A proposed scheme for the DOS redistribution of the Ni and Cr 3d bands occurring upon formation of the AlCoCrCuFeNi HEA. Reproduced from ref. 65 with permission from Elsevier.

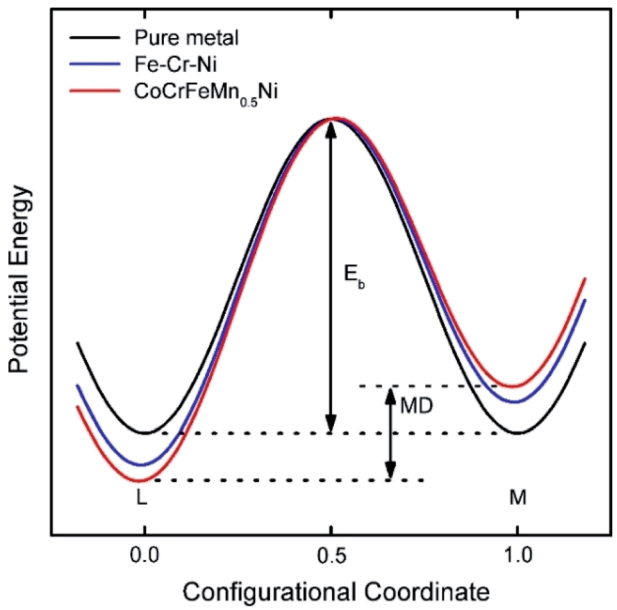

Fig. 10 Schematic diagram of the variation of low-potential energy and mean difference (MD) during the migration of a Ni atom in different matrices. The MD for pure metals is 0, whereas that for HEA is the largest.[67] Reproduced from ref. 67 with permission from Elsevier.

conditions, elements contained in HEAs, crystal phase and morphology, substrate applicability, duration time and elemental distribution. Most of the current methods require rigorous conditions including low pressure, temperature and inert atmospheric protection. Under such experimental conditions, HEA NPs are only immobilized on limited thermally resistant substrates (*e.g.* carbon, γ-Al_2O_3, zeolite) rather than thermally sensitive ones (*e.g.* metal foam, glass, polymer, which are often used in many applications). While some synthesis methods, such as electrosynthesis and pulsed laser ablation, yield HEAs under mild conditions, they either require targets with the same composition as the HEA NPs, or only craft amorphous NPs, narrowing the varieties of HEAs. On the other hand, it is clearly found that HEAs with good elemental distribution are generally synthesized in a short period of time, even microseconds. It is understandable that the high mixing entropy property of HEAs contributes to solid solution formation at high temperatures due to $T\Delta S_{mix}$. In the slow cooling process, segregation or precipitation of the second phase may occur due to decreased $T\Delta S_{mix}$, thus forming heterogeneous microstructures. A faster cooling rate can suppress the formation of secondary phases, and tend to create single-phase HEAs with good elemental distribution.

3. Core effects of HEAs

The multi-elemental character of HEAs leads to some important effects that are much less pronounced in conventional alloys.[46] Among these, four core effects including high entropy, cocktail, sluggish diffusion and lattice distortion are more basic.[47] This section will briefly introduce the core effects as well as their impact on the catalytic properties of HEAs.

3.1 High entropy effect

Based on Boltzmann's hypothesis, the configurational mixing entropy (ΔS_{mix}) can be expressed as:[48]

$$\Delta S_{mix} = -R\sum_{i=1}^{n} c_i \ln c_i$$

where n is the number of principal elements, R is the gas constant, and c_i is the mole fraction of component i. The relationship between the ΔS_{mix} value and the number of principal elements mixed in equimolar ratio is shown in Fig. 7a and b. In a broad sense, $1.5R$ is used as a border line between HEAs and medium-entropy alloys.[49] Since the growth rate of ΔS_{mix} slows down after a 9-element alloy, HEAs with 5 to 9 components are suggested in practical application.[49,50] More components will not benefit from high entropy but increase the material complexity.

The characteristic of high mixing entropy enhances the mutual solubility among elements and facilitates the formation of simple FCC, BCC or HCP solid solution phases within HEAs during solidification (Fig. 7c).[50] Cantor *et al.* manufactured

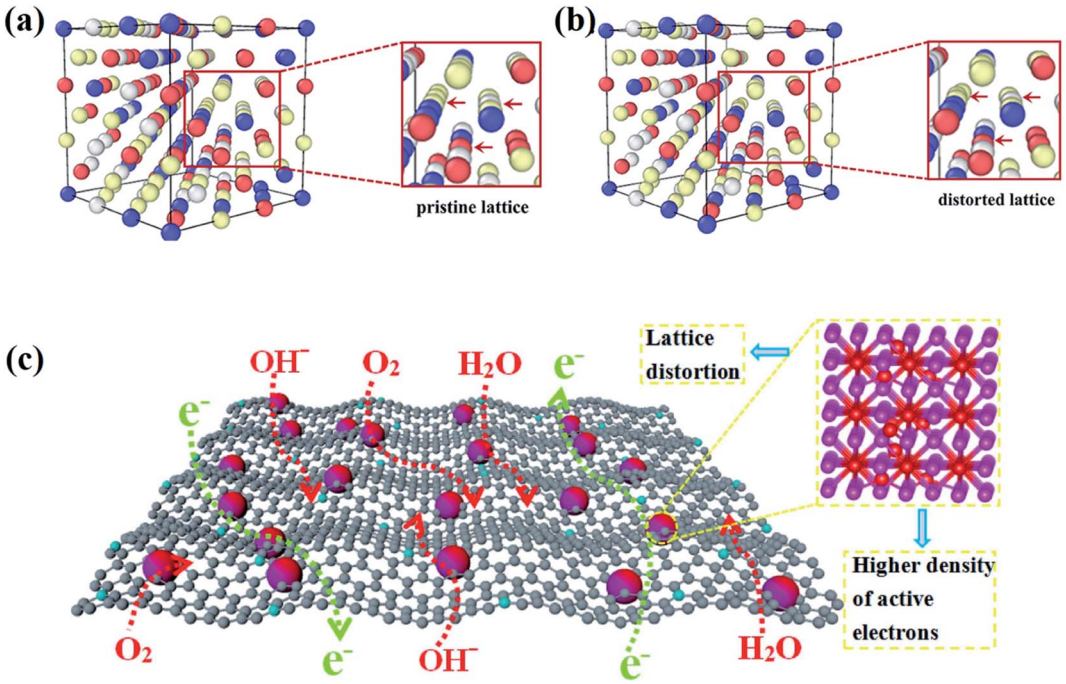

Fig. 11 The DFT simulation results of (a) the pristine lattice with an ideal FCC structure and (b) the distorted lattice of the CoCrFeNi alloy. Reproduced from ref. 68 with permission from Frontiers. (c) Schematic of the advantages of the lattice-distortion alloys for bifunctional oxygen electrocatalysts.[69] Reproduced from ref. 69 with permission from Elsevier.

transition-metal-rich HEAs with six to nine components (the same five elements of Fe, Co, Ni, Cr, and Mn together with other elements such as Cu, Ti, Nb, Ni, Mo, Ta and Ge) in equal atomic ratio, which also forms a single FCC solid solution.[52]

In principle, HEAs with a solid solution phase have many merits that can justify them as great potential catalysts. Firstly, they can be produced with wide composition ranges not available in the crystalline form, permitting the fine tuning of their electronic properties to meet catalytic reaction demands.[53] Under the definition of HEAs which consist of more than five elements, we can obtain a total of 7099 possibilities for designing equal-mole HEA systems at an arbitrary choice of a group of 13 metallic elements.[49] Unequal-mole HEAs may also be designed with minor alloying elements like $AlCo_{0.5}CrCuFe_{1.5}Ni_{1.2}B_{0.1}C_{0.15}$ for further modification of the microstructure and electronic properties. As a result, HEAs offer researchers even more room for design in terms of their composition and electronic properties than traditional alloys. Secondly, the isotropic and homogeneous characters of the alloys allow the active sites in a chemically identical environment. For HEAs, their single-phase character and lack of surface segregation of the alloying elements ensure that the catalytically active species are dispersed uniformly, which would benefit the development of the HEA catalysts with high and exclusive selectivity.[54] Thirdly, the high entropy effect has been considered to be the main reason for the stability of HEAs. The increase of the number of components significantly increases the configurational entropy, and leads to phase stability *via* a decrease of the Gibbs free energy.[3] It has been reported that the HCP phase of HEA catalysts (IrOsReRhRu) is still retained after heat treatment up to 1500 K and compression to 45 GPa, achieving a record temperature and pressure stability for a single-phase HEA.[55] Due to the large difference in compressibility between Os and other metals, the HEA has higher thermal expansion and lower bulk modulus in comparison with the pure metals in the compositions.[55] In the electrocatalytic oxidation of methanol, the simple-phase character and the high mixing entropy of the elements in HEAs ensure that the active sites are in a uniform dispersion in a homogeneously chemical environment, thus showing pronounced electrocatalytic activity.[55] In the nanostructures of HEA-CoMoFeNiCu, the five principal components are initially randomly assigned to each lattice site, forming a simple FCC phase. Such a solute–solution mixing phase prevents a large miscibility gap which presents in a bimetallic Co–Mo alloy.[56] As shown in Fig. 8, the randomly mixing surface with uniform distribution of Co and Mo sites optimizes both the dehydrogenation of NH_3 molecules and the desorption of the product N_2 from the HEA surface in the catalytic decomposition reaction of NH_3.[56]

3.2 Cocktail effect

HEAs can be considered as composite materials at the atomic scale due to their multi-elemental character. Their properties are certainly related to not only the properties of the individual composing principal elements, but the interaction among the elements. In other words, some unexpected properties may be obtained after mixing many elements, which would not manifest using any one independent element. For example, although Al is a soft and low-melting-point element, the addition of Al

Table 2 Catalytic applications of HEAs and the mechanisms for the improved performance

HEAs	Phase	Synthetic method	Reaction	Mechanisms for improved performance	Ref.
PtFeCoNiCuAg	FCC	Sputter	Electrocatalytic methanol oxidation	Not mentioned	70
PtNiCoCuFe	Not mentioned	Electrosynthesis	Electrocatalytic methanol oxidation	Resistance to the poisoning of carbonaceous species	71
IrOsReRhRu	HCP	Pyrolysis	Electrocatalytic methanol oxidation	Not mentioned	55
NiNbPtSnRu	Amorphous	Mechanical milling	Electrocatalytic methanol and CO oxidation	Lower rate of poisoning	72
PtRuCoOsIr	FCC + HCP	Dealloying	Electrocatalytic methanol oxidation and the ORR	The downshift of the Pt d-band weakens the O–O bond	73
AlCoCrTiZn	BCC	Mechanical milling	Catalytic degradation of azo-dyes	Lattice distortion and residual stress lead to a low activation energy barrier	74
AlCrFeMnTi	FCC + BCC	Mechanical milling	Catalytic degradation of azo-dyes	The presence of plenty of nano-galvanic cells among the principal elements	75
AuAgPtPdCu	FCC	Mechanical milling	Electrocatalytic CO_2 reduction	Destabilization of *OCH_3 intermediates and the strong stabilization of *O intermediates	9
NiFeMoCoCr	FCC or FCC + μ	Arc-melting	Electrocatalytic HER	High coordination numbers of single-phase FCC promote the hydrogen adsorption	66
FeCoPdIrPt	FCC	Moving bed pyrolysis	Electrocatalytic HER	The downshift of Pt antibonding states facilitates hydrogen species desorption	24
IrPdPtRhRu	FCC	Polyol method	Electrocatalytic HER	Deeper d-band centre locations (between Ir and Pt)	76
MnFeCoNiCu	FCC	Solvothermal-pyrolysis	Electrocatalytic OER	The presence of lattice defects contributes to the catalytic activity	21
AlNiCoFeX (X = Mo, Nb, Cr)	FCC	Top-down synthesis	Electrocatalytic OER	X atoms prefer high formal oxidation states, facilitating proton migration to O at Ni/Co sites	77
CoFeLaNiPt	Amorphous	Electrosynthesis	Electrocatalytic HER and OER	Synergism between Pt and the other elemental components on the atomic scale	6
PtAuPdRhRu	FCC	Wet chemistry	Electrocatalytic HER and OER	High-entropy at the nanoscale and strong synergistic effects between active metals	32
AlNiCoIrMo	FCC	Dealloying	Electrocatalytic HER and OER	The increased covalency of Ir–O bonds by alloying	36
CrMnFeCoNiNb	Not mentioned	Sputter	Electrocatalytic ORR	Solid solution phase with altered properties overcomes the limitations of the single elements	78
AlCuNiPtMn	FCC	Dealloying	Electrocatalytic ORR	The best electronic modulation for the Pt surface through surface strain and/or ligand effects	79
PtPdFeCoNi	FCC	Carbothermal shock	Electrocatalytic ORR	Rapid electrochemical screening is demonstrated by using a scanning droplet cell	80
Hollow RuIrFeCoNi	FCC	Droplet-to-particle	As the cathode catalyst for Li–O_2 batteries	Maximizing the material usage efficiency by tuning the HEA shell thickness	2
FeCoNiCuMo	FCC	Carbothermal shock	Thermocatalytic NH_3 decomposition	Tunable surface adsorption properties by varying the Co/Mo ratio	56
RuRhCoNiIr	FCC	Carbothermal shock	Thermocatalytic NH_3 decomposition	A synergistic effect from multiple elements, ultrafine size, and homogeneous structure	1
PtPdRhRuCe	FCC	Carbothermal shock	Thermocatalytic NH_3 oxidation	Homogeneous nature of the solid-solution NPs	18

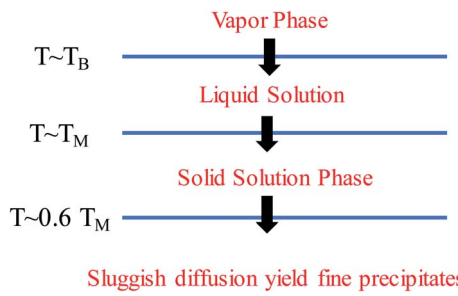

Fig. 12 Phase transformation during the solidification of an HEA.

can dramatically harden CoCrCuNiAl HEAs due to the formation of a hard BCC phase as well as the stronger cohesive bonding between Al and other elements.[3,57,58] This phenomenon is called the "cocktail effect", which was first mentioned by Ranganathan[59] and then confirmed *via* the mechanical properties.[60–62]

The multi-metallic cocktail effect can optimize the electronic structures of catalysts. In HEA systems containing Ni and Pd, the electron transfer from Ni to Pd could occur due to the smaller electronegativity of Ni than Pd, which can decrease the Pd–CO binding energy and enhance the catalytic oxidation of methanol molecules.[63] Moreover, the electronic states of metal atoms are altered by alloying with the d-band center of Pd shifting down and the d-band center of Ni shifting up,

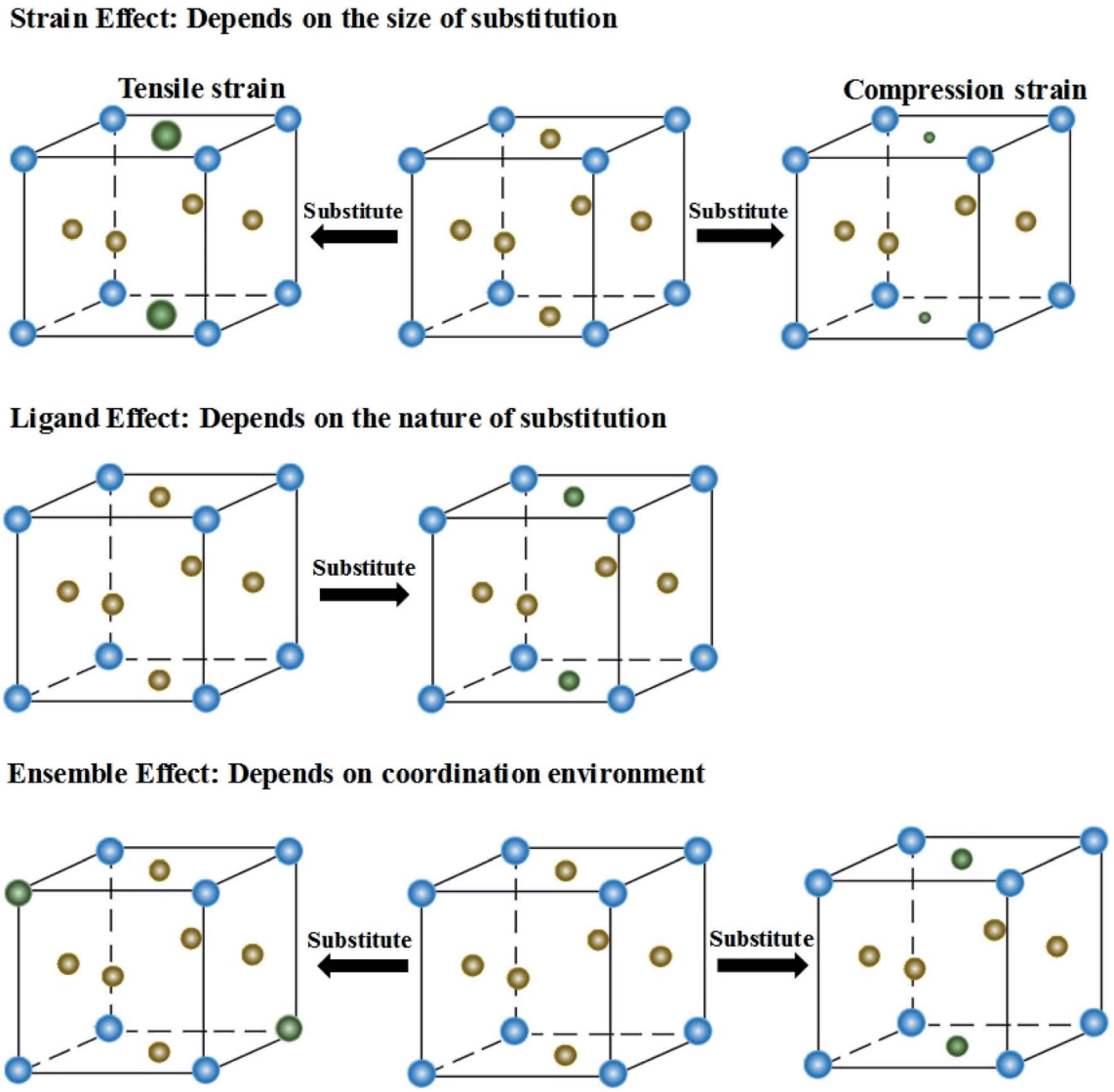

Fig. 13 Three substitution effects in alloys: strain, ligand and ensemble effects.

promoting the electrocatalytic activity of Pd towards methanol/ethanol oxidation and enhancing the adsorption of adsorbates on the Ni sites.[64] The cocktail effect can also alter the charge transfer and chemical ordering of HEAs, as shown in Fig. 9. In an AlCoCrCuFeNi HEA, the occupied and empty Ni 3d states shift away from the Fermi level, whereas the Cr 3d empty states shift towards the Fermi level, compared to the corresponding pure metals.[65] The charge transfer between the elements in HEAs is negligible due to the compensation of the 3d state occupancy change by the redistribution of delocalized 4s and 4p states of the transition metals.[65] These properties play important roles in the optimization of the adsorption energy of HEAs during catalytic reactions.

In a word, the cocktail effect in HEAs is generally considered as a complex synergetic mechanism that is responsible for the outstanding catalytic performance of HEAs. The synergistic interactions of the multi-element compositions in HEAs have resulted in a huge divergence of the properties as compared to atoms in single-element metals. But the remarkable thing is that the mechanism of action of such multi-component synergy in HEAs remains largely unknown. The underlying synergistic mechanisms from the view point of lattice distance and electron distribution should be further explored.

3.3 Sluggish diffusion effect

Diffusion refers to the phenomenon wherein atoms vibrating at the lattice equilibrium absorb energy at high temperatures and migrate away from their original positions. In phase transformations controlled by diffusion, the formation of a new phase usually requires the cooperative diffusion of elements to attain the equilibrium partition among the phases. Each principal component in HEAs usually presents a highly chaotic state due to the high entropy of the mixing effect. The principal atoms in HEAs can be regarded as either solute or solvent atoms, which increase the resistance of atomic diffusion and reduce the atomic diffusion rate. The phase separation is

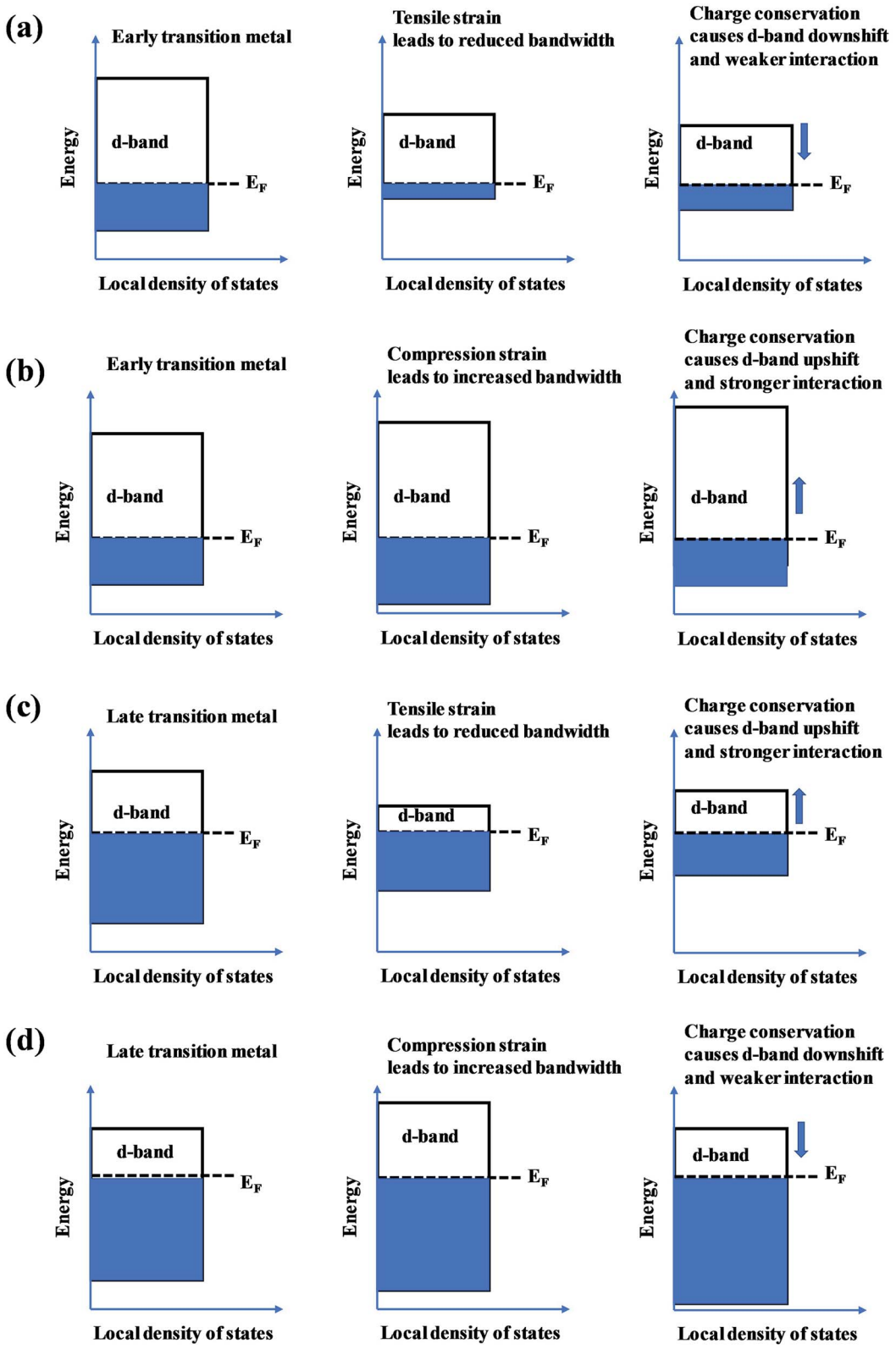

Fig. 14 The effect of (a and c) tensile and (b and d) compression strain on the position of the d band in early transition metals and late transition metals.

inhibited, and the nucleation and growth of new phases are suppressed. This phenomenon is known as the sluggish diffusion effect on the kinetics of HEAs.

The sluggish diffusion effect of HEAs can suppress the degradation caused by the coarsening of nanostructured HEA catalysts.[35,66] Despite the poor corrosion resistance of pure

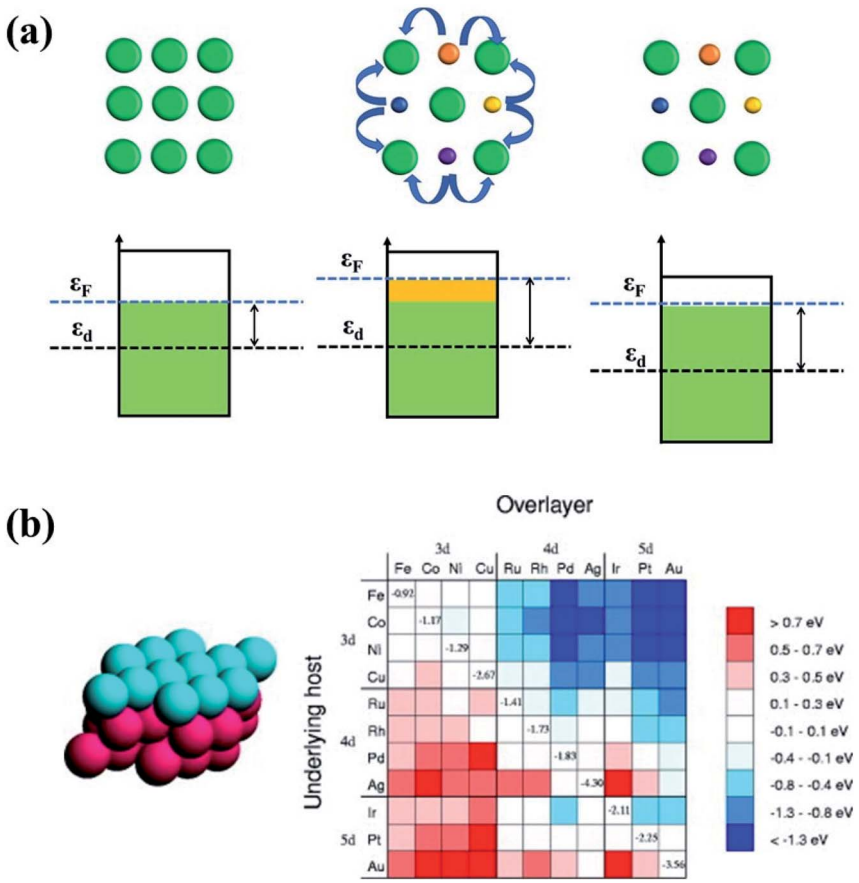

Fig. 15 (a) The ligand effect of HEAs and the d-band center shift. The green balls represent noble metal atoms. The orange, purple, blue and yellow balls represent non-noble metal atoms. (b) Changes in the d-band centers for monolayer overlayer on transition metal substrates. Reproduced from ref. 125 with permission from Elsevier.

transition metals in strong acid or alkali solution, the high entropy alloy $Ni_{20}Fe_{20}Mo_{10}Co_{35}Cr_{15}$ composed of such elements showed high corrosion resistance in both acidic and basic electrolytes for the hydrogen evolution reaction (HER).[66] The reasons for the sluggish diffusion effect of HEAs are still controversial. Most of the researchers hold the view that multiple components are responsible for the sluggish diffusion due to low lattice-potential-energy sites provided by small atoms.[35,67] HEAs with multiple principal elements have larger fluctuations in lattice potential energy than pure metals or traditional alloys (Fig. 10). Many low lattice-potential-energy sites always serve as atomic traps and blocks.[67] Thus, if an atom jumps to a low-local-potential state, it would have a low possibility to jump out. In contrast, if an atom jumps to a high-local-potential state, it would have a high chance to hop back to the initial site. Both cases can hinder atomic diffusion and particle coarsening due to the increased energy barrier and activation energy for diffusion. Meanwhile, some other researchers think that certain elements, such as Mn in CoCrFeMnNi alloy, produce a deep potential wall and thus cause a sluggish effect.[67] Therefore, a thorough study should be performed to clarify the origins of the sluggish diffusion effect of HEAs, which in turn helps researchers better design the overall architecture of high-performance HEA catalysts.

3.4 Lattice distortion effect

HEAs are composed of various elements with different sizes, leading to the lattice distortion effect (Fig. 11a and b).[68] Larger atoms tend to push away their neighbors to occupy more space, whereas small ones are distributed in extra space. The large atoms lead to compression, whereas small ones result in tension strain in the lattice. The bonding energy between atoms is another factor that causes the lattice distortion. Stronger bonds are prone to have smaller bonding distances than weaker bonds. The lattice distortion effect in HEAs is claimed to be more severe than in conventional alloys. If the differences in the properties and structures of the principal elements are large enough, the distortion of the material system will be too severe to maintain the original stable lattice, and the collapse will occur to form an amorphous structure. The lattice distortion effect can affect the mechanical, chemical and physical properties of HEAs.

It was reported that the lattice distortion in an Fe-enriched alloy promoted a higher density of active electrons around the Fermi level (Fig. 11c).[69] The higher density of activated electrons results in faster electron transfer. In contrast, the electron transfer in alloys with a pristine lattice is quite limited due to the absence of activated electrons. Thus, the alloys with lattice

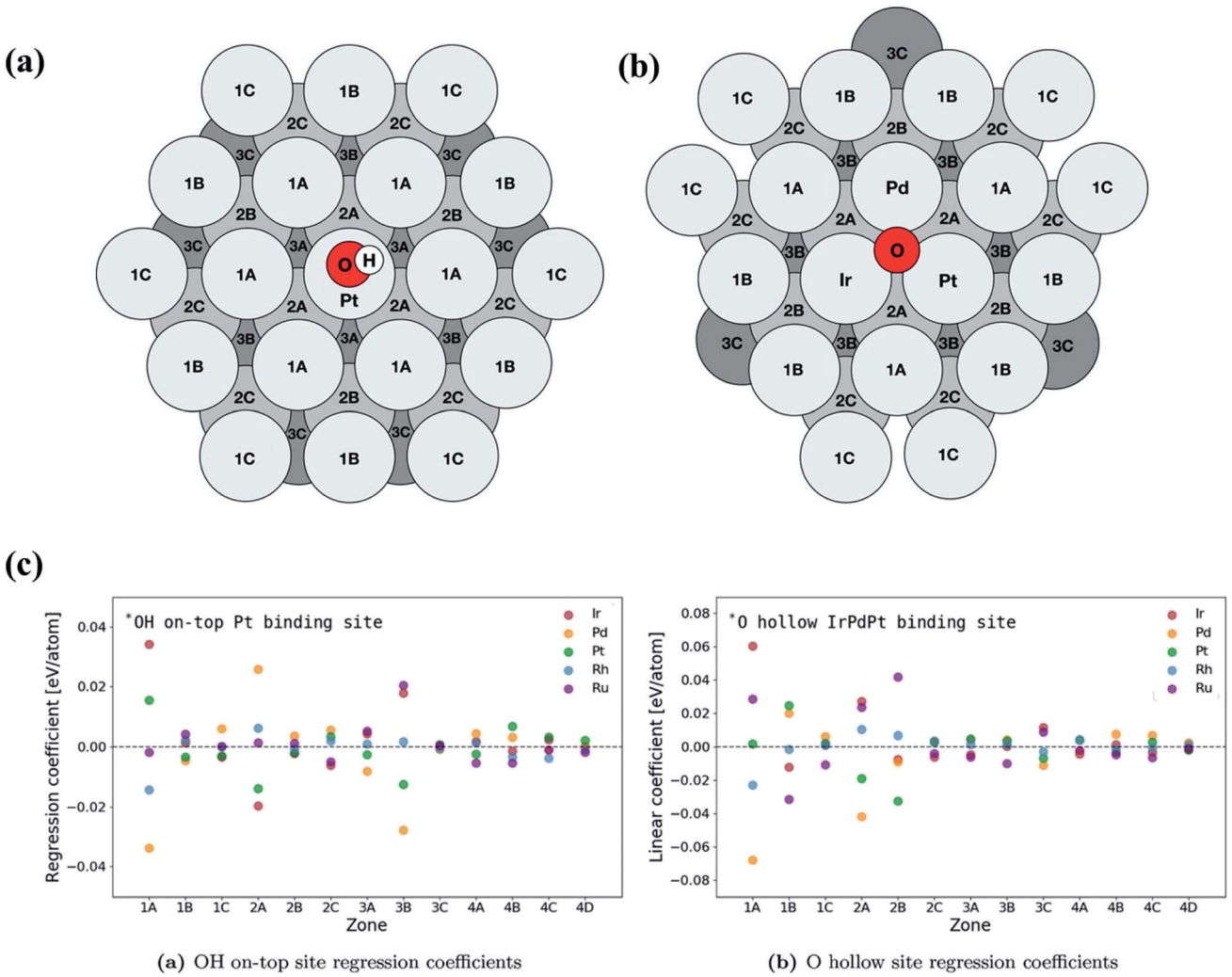

Fig. 16 Schematic of atomic positions grouped by layer and distance from the binding site on an FCC (111) surface microstructure for (a) on-top adsorption on Pt and (b) fcc hollow site adsorption on IrPdPt. The fourth layer contains zones 4A, 4B, 4C and 4D and has an identical layout to the first layer. (c) Overview of the regression coefficients of the least squares fits for each element by zone. The atoms with direct coordination (*i.e.*, zones 1A and 2A) to the binding atoms have a large effect on the binding energy of the intermediate. Zone 3B has a similar sized impact on the binding energy to the neighbors in zone 2A. Reproduced from ref. 126 with permission from John Wiley and Sons.

distortion showed improved catalytic performance than alloys with a pristine lattice in catalysis, such as the oxygen evolution reaction (OER) and oxygen reduction reaction (ORR).[69] Moreover, some metastable structures (namely fragmented domains such as short-range order, critical defects, amorphous structures, *etc.*) may form to accommodate the lattice distortion effect during the preparation of HEAs.[1] Such metastable microstructures are believed to play a key role in enhancing the catalytic performance of HEAs. Lattice distortion can also induce a residual strain field with atomic scale fluctuation, shift the d-band center of catalysts and ultimately affect the catalytic selectivity. The effects of these microstructures and strain on the catalytic performance of HEA catalysts are discussed in detail in Section 3.2 and 3.3, respectively.

In brief, the high-entropy effect simplifies the microstructures of HEAs to form simple solid solution phases, leading to the homogeneous distribution of active site configurations in catalysis. The cocktail effect causes a synthetic effect on properties, wherein the interactions among the different elements may optimize the adsorption energy of the intermediates, thereby enhancing the catalytic activity. The sluggish diffusion effect increases the activation energy and reduces the coarsening kinetics in the grain growth process. It enhances the thermal and chemical stability of HEAs in catalysis. The lattice distortion effect has a great impact on the physical and chemical properties of HEAs, which often results in severe strain due to the atomic size mismatch. Such a strain potentially shifts the d-band center of alloys, and affects the binding modes of intermediates as well as the catalytic selectivity. Moreover, some possible metastable microstructures in the solid-state solution phase of HEAs may form during the preparation process due to the lattice distortion effect, which holds promise for providing a variety of active sites in catalysis.

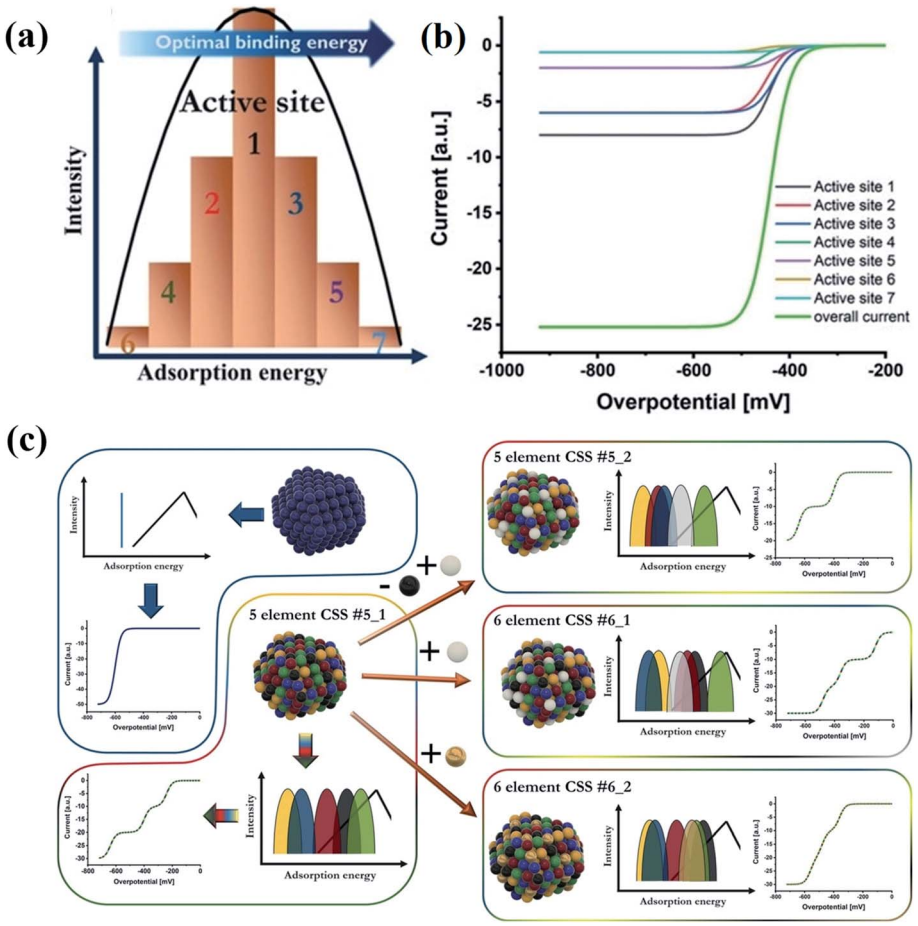

Fig. 17 (a) Scheme of active site distribution within one adsorption peak. (b) Visualized intrinsic current response in the kinetic region of these grouped active sites, considering their activity as well as the intensity. (c) Scheme of correlations between a complex solid solution (CSS) NP structure, its effect on the adsorption energy distribution pattern, and the respective electrochemical response in the kinetic region. Reproduced from ref. 132 with permission from John Wiley and Sons.

4. Core effect-induced properties for highly efficient HEA catalysts

The four core effects, discussed in Chapter 3, play crucial roles in determining the properties of HEAs such as metastable microstructures, strain, ligand and ensemble effects, d-band center, and adsorption energy. Microstructures of HEAs (*e.g.* amorphous/intermetallic precipitates, short-range orders, vacancies, grain boundaries) induce strain, ligand and ensemble effects which then affect the position of the catalyst d-band center. The d-band shift has a significant impact on the optimization of the adsorption energy of the reactants, which is responsible for the high catalytic activity of various reactions. To date, HEA catalysts have been involved in reactions including electrocatalysis (*i.e.* methanol and CO oxidation, CO_2 reduction, HER, OER and ORR), thermocatalysis (*i.e.* NH_3 decomposition and NH_3 oxidation), and catalytic degradation of azo-dyes at room temperature. These catalytic applications of HEAs and the mechanisms for the improved performance have been summarized in Table 2. This chapter mainly discusses the relationship between these properties of HEAs in detail as well as their impacts on the catalytic performance of catalysts in these reactions.

4.1 Metastable microstructures

It should be clarified that mixing entropy is generally compared in the random solid-solution state or liquid solution. Compared with conventional alloys, HEAs have high mixing entropies in these states. The solidification process determines the microstructure formation of HEAs. Fig. 12 shows the phase transformation during the solidification of an HEA.[49] The high mixing entropy effect of HEAs facilitates the formation of the solid solution phase at high temperature due to $T\Delta S_{mix}$. During subsequent cooling, segregation or precipitation of the second phase may occur because mixing entropy becomes less important. However, the sluggish diffusion effect of HEAs leads to the production of fine microstructures. A faster cooling rate can suppress the precipitation of the second phase to form the solid-solution or amorphous phase, whereas a slower cooling rate would create intermetallic phases. Because the high configurational entropy effect is often insufficient to fully stabilize a single-phase solid solution in the presence of lattice

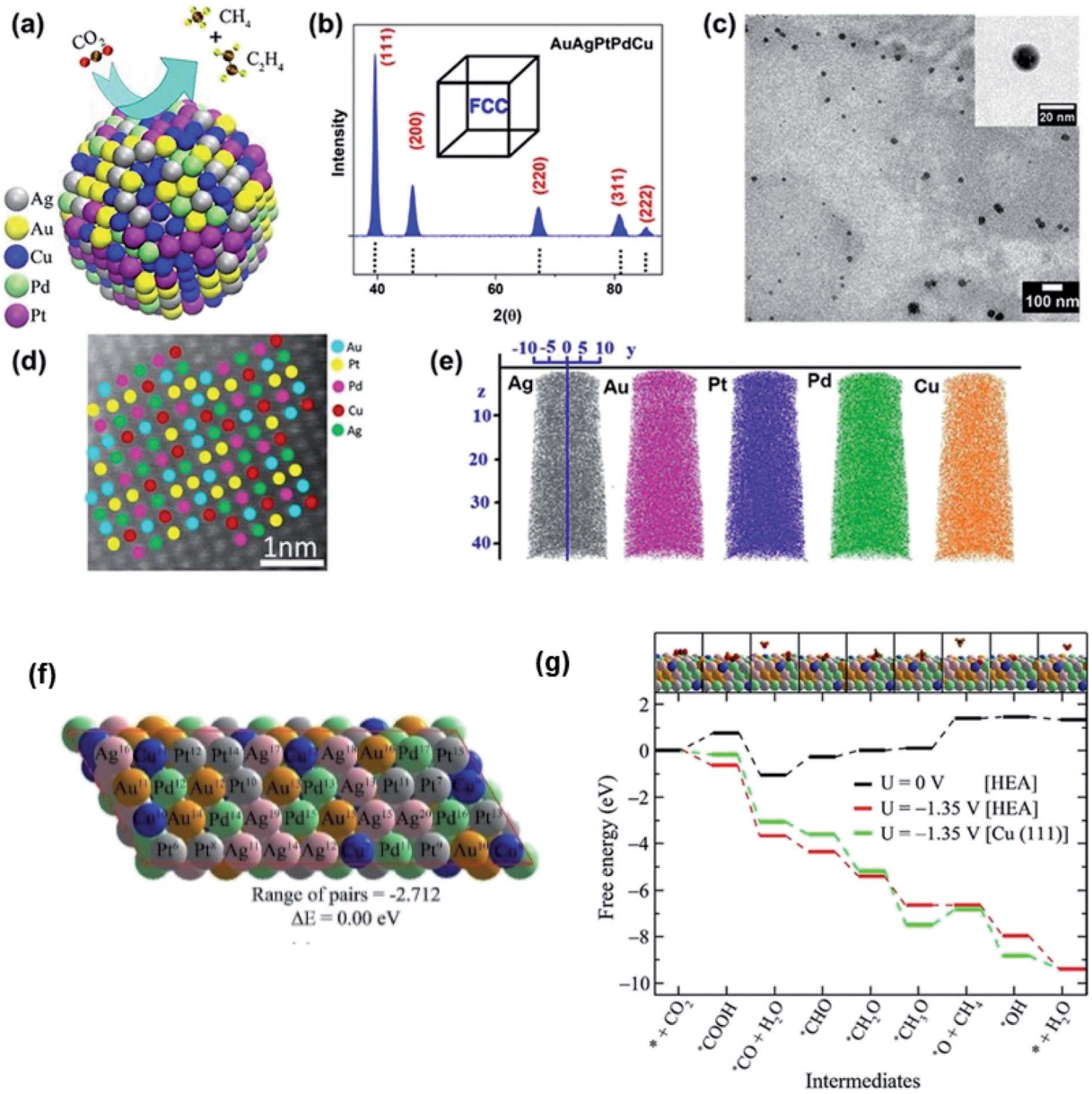

Fig. 18 (a) Schematic of the electrocatalytic reduction of CO_2 on the surface of a AuAgPtPdCu HEA. (b) X-ray diffraction (XRD), (c) transmission electron microscopy (TEM) bright-field image, and (d) high-resolution scanning transmission electron microscopy (HR-STEM) image of AuAgPtPdCu HEAs; the inset of (c) shows a high magnification image of a single AuAgPtPdCu HEA nanoparticle. (e) Chemical homogeneity of Au, Ag, Pt, Pd, and Cu. (f) Optimized structure of the special quasi-random structure of the AuAgPtPdCu HEA. (g) Free-energy diagram of CO_2 reduction reaction on the AuAgPtPdCu surface. The inset shows the optimized structures of the intermediates on the HEA surface. Gray, green, pink, yellow, blue, brown, red, and orange spheres represent Pt, Pd, Ag, Au, Cu, C, O, and H atoms, respectively. Reproduced from ref. 9 with permission from the American Chemical Society.

strain enthalpies or structural mismatch of components, metastable microstructures, such as amorphous/intermetallic precipitates, short-range orders, vacancies, and grain boundaries, are inevitably formed during the preparation of HEAs.[81,82] These fine metastable microstructures disrupt the local chemistry and cause heterogeneity in HEAs. The types and density of the microstructures are closely related to the synthetic techniques.

An interesting issue arises regarding the functions of the metastable microstructures in catalytic reactions. Alloys with these microstructures have coordinatively unsaturated sites which are essential for the bonding and activation of the reactants. HEAs have a high concentration of coordinatively unsaturated metal centers (active sites), which makes adsorption[83] and surface reactions[84] easier than on the corresponding crystalline catalysts. Although the effect of such microstructures on the catalytic properties of HEAs has not yet been reported in the literature, their functions in traditional metal/alloy-based catalysts have been demonstrated in detail.[85–87] It has been reported that the presence of unsaturated Ni(II) binding sites in a nano-

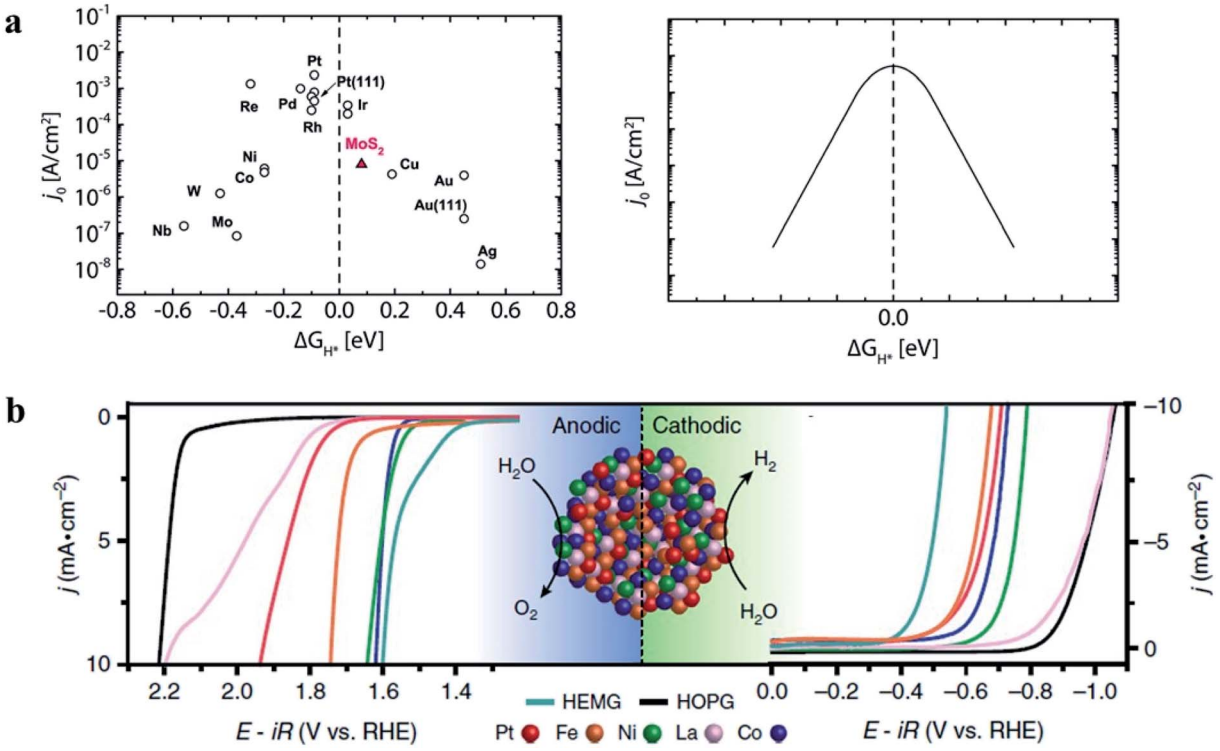

Fig. 19 (a) Current density as a function of hydrogen adsorption energy.[134] Reproduced from ref. 134 with permission from the American Chemical Society. (b) Electrocatalytic O_2 and H_2 evaluation of a CoFeLaNiPt HEMG-NP (High-Entropy Metallic Glasses-nanoparticle) electrocatalyst. Each material was loaded onto the HOPG (highly oriented pyrolytic graphite) substrate. Reproduced from ref. 6 with permission from Springer Nature.

porous hybrid material significantly improved hydrogen sorption quantity compared with that of similar materials without unsaturated metals sites.[83] A silver catalyst with stacking faults (defects) and a low coordination number showed superior activity of the hydrogen evolution reaction that outperforms commercial platinum on carbon which is usually considered as the best catalyst.[88] These sites make the adsorption and surface reactions of catalytic intermediates easier than conventional crystalline catalysts, ensuring a high catalytic activity. Catalytic doping of alloys is an effective avenue to improve the hydrogen-storage property of MgH_2. Compared with crystalline HEAs, amorphous counterparts exhibited better kinetics and lower activation energies during MgH_2 catalysis due to a more uniform distribution of highly refined nanostructures in the amorphous phase.[77] The amorphous alloy catalysts become brittle by absorbing hydrogen, which is beneficial to the formation of refined nanostructures. Consequently, the presence of an amorphous HEA catalyst with the refined nanostructures accelerates hydrogen diffusion in the Mg/MgH_2 matrix, thus enhancing the hydrogen storage properties of MgH_2. In addition, as the metastable structures are nonporous, the surface reaction would not be affected by diffusion limitations, which is often a problem in traditional heterogeneous catalysis.[89] All these features make HEAs with metastable microstructures attractive in heterogeneous catalysis.

4.2 Relationships of strain, ligand and ensemble effects with the d-band of HEAs

The presence of the metastable microstructures can affect the lattice constant (strain effect), spatial arrangement of different elements (ligand effect), and alloy geometries (coordination effect).[90] These three effects are considered to tune alloy surface properties and play significant roles in the improvement of catalyst activity. As shown in Fig. 13, the strain effect depends on the size of the substituted atom, the ligand effect relies on the nature of the substitution, and the ensemble effect is related to the coordination environment of atoms. This section describes the three effects in detail, and their relationships with the HEA d-band are also discussed.

4.2.1 The strain effect and d-band center. The strain effect in alloys is more pronounced for atoms with different radii, where phase segregation may occur and one phase stretches or compresses the neighbors to induce tensile or compressive strain. Such strains can lead to the d-band center shift, thus perturbing the adsorption energies of intermediates during catalytic reactions. Structurally, each atom in HEA solid solutions is surrounded by different metal atoms, and each principal component has the same probability of distribution in the crystal lattice sites of the phases. In the FCC and BCC phases, different principal elements tend to occupy different sets of lattice sites. The displacement at each lattice site depends on the discrepancies in atomic size, chemical properties and

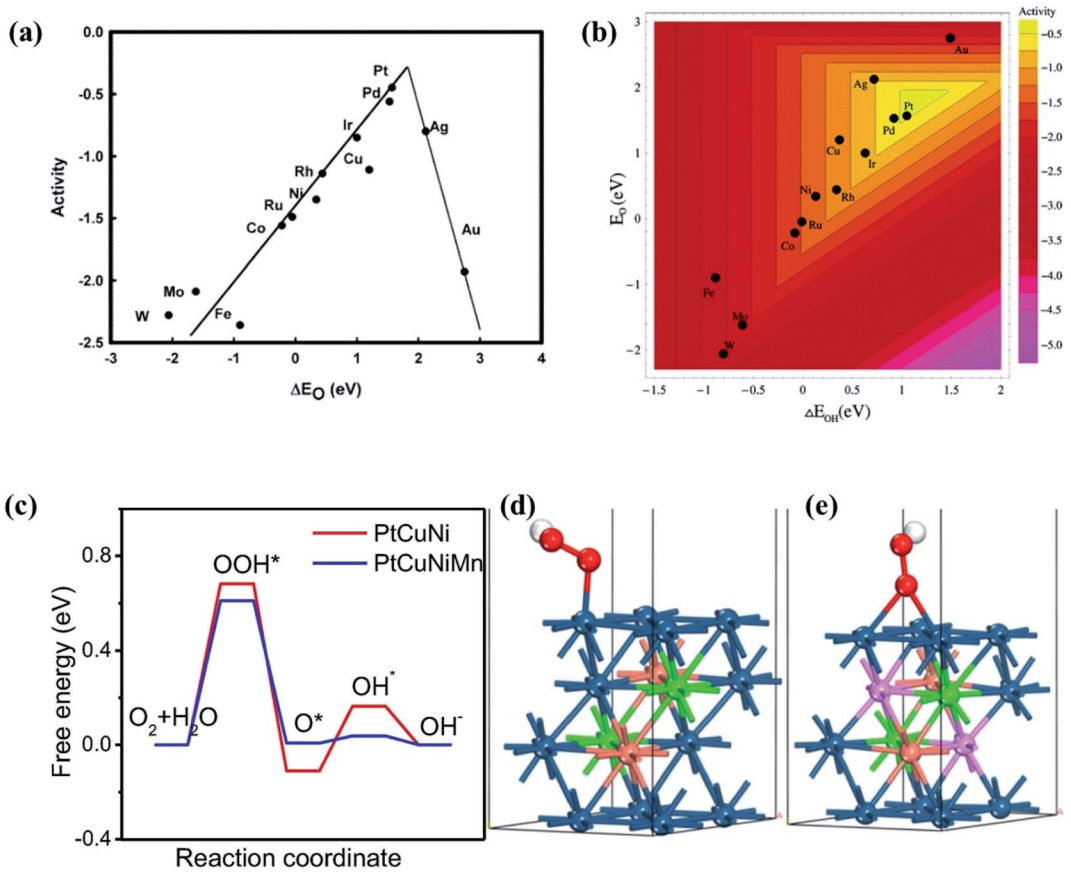

Fig. 20 Trends in ORR activity as a function of (a) the O adsorption energy or (b) both the O and the OH binding energy. Reproduced from ref. 136 with permission from the American Chemical Society. (c) Free energy profiles of the ORR steps on the PtCuNiMn and PtCuNi. Adsorption configurations of the OOH on the (d) PtCuNi and (e) PtCuNiMn models. The colors dark blue, pink, brown, green, red and white represent the atoms of Pt, Mn, Cu, Ni, O and H, respectively. Reproduced from ref. 79 with permission from Elsevier.

structural characteristics of atoms in HEAs. These lattice distortions are claimed to create surface strains that can be calculated and analyzed statistically.[50,91]

The mechanical behavior of catalysts is one of the most important factors for the reliable and efficient catalytic reactions, and understanding the role of surface strain in tuning the reaction is critical for catalyst design.[92–97] For instance, as-exfoliated monolayered WS_2 nanosheets exhibited enhanced electrocatalytic activity for hydrogen evolution due to the high concentration of the strained metallic 1T phase.[98] In principle, strain modifies the physical/chemical properties of catalyst surfaces by changing the average energy of the d band.[99] The width of the surface d band was found to be proportional to the interatomic matrix element that describes bonding interactions. The misfit strain changes the width of the d band through changes in the d-orbital interactions between the d orbitals of a metal atom and the d orbitals of its nearest neighbors that are quite sensitive to interatomic spacing.[100] As a consequence of the d width change, the average energy of the d band (the d-band center) moves down or up relative to the Fermi energy in order to maintain a constant d-band filling, resulting in modifications of the strained surface properties. On the basis of the theoretical simulations, the d-band center of catalysts play an important role in their catalytic activity because the d-orbital electrons determine both bond formation and breaking of the intermediate species.[101,102] According to the d-band model,[103] the position of the d-band center determines the adsorption energies and activation energy barriers. The shift of the d-band center influences the bonding and anti-bonding states of adsorbates and reactants on the alloy catalyst surface, and further determines the activity and selectivity of catalytic reactions.[104] To achieve optimal catalytic activity, the d-band center must not be too close or too far from the Fermi level. Notably, the shift trend of the d-band center is reverse for late transition metals (LTMs, for which the d bands are more than half filled) and early transition metals (ETMs) with a less than half-filled d band. Fig. 14 shows the influence of tensile strain on the position of the d band in ETMs and LTMs.[105] ETMs exhibited lower adsorption energies under tensile strain because the expanded lattice reduced the overlap of the wavefunctions and therefore narrowed the metal d band, in contrast to what is observed in LTMs.[105,106] The band narrowing results in an increased population of the d band of LTMs, upshifting the d-band center to preserve the degree of d-band filling. Yan *et al.* proved that the influence of externally applied elastic strain on the catalytic activity of metal films in the hydrogen evolution

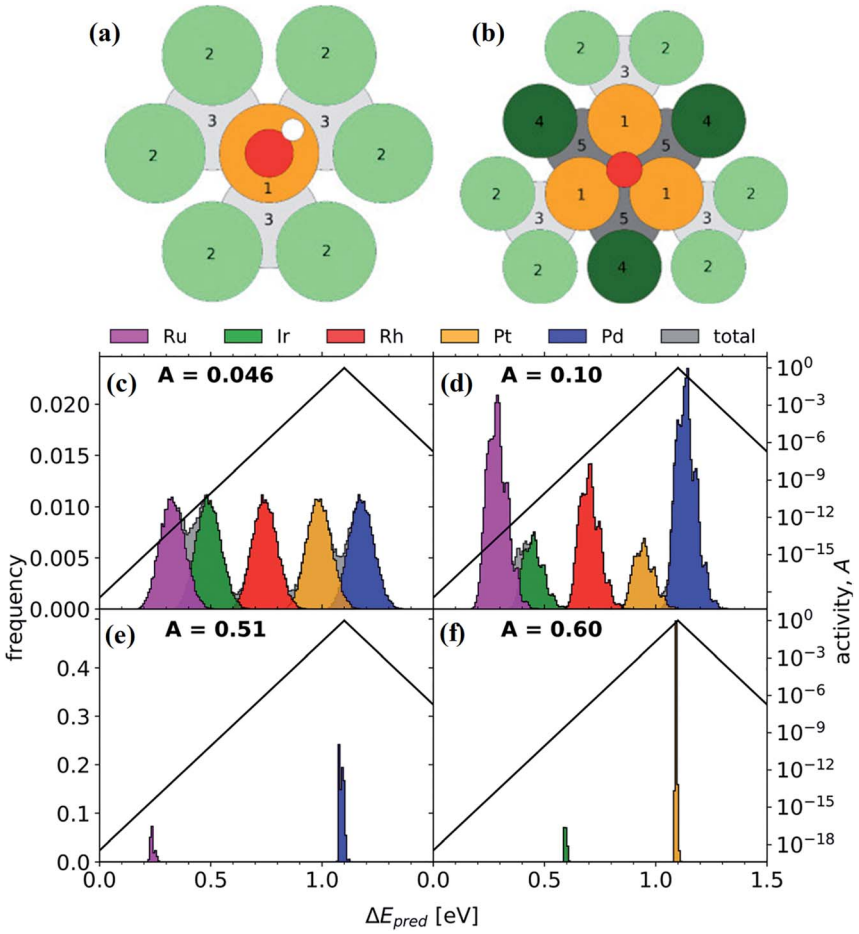

Fig. 21 (a) *OH on-top binding. Orange (1): binding site. Light green (2): surface neighbors are coordinating once to the binding site. Light gray (3): subsurface neighbors are coordinating once to the binding site. (b) *O FCC hollow site binding. Dark green (4): surface neighbors are coordinating twice to the binding site. Dark gray (5): subsurface neighbors coordinating twice to the binding site. Distribution of adsorption energies for (c) $Ir_{20}Pd_{20}Pt_{20}Rh_{20}Ru_{20}$, (d) $Ir_{10.2}Pd_{32.0}Pt_{9.30}Rh_{19.6}Ru_{28.9}$, (e) $Pd_{81.7}Ru_{18.3}$, and (f) $Ir_{17.5}Pt_{82.5}$ (global maximum activity). *A* represents the activity. Reproduced from ref. 141 with permission from Elsevier.

reaction (HER) is in a controlled and predictable way.[107] The activities of Ni and Pt were accelerated by compression, while that of Cu was accelerated by tension.[107] Pt-based catalysts exhibited intensive adsorption for catalytic intermediates in the HER and ORR, which was weakened by introducing compressive strain through interface mismatch or size reduction.[108–111] It has been reported that a surface strain of −2.0% would be the best for Pt-based alloy catalysts toward the highest ORR activity.[112,113] DFT has proven that a Pt layer with −2.0% strain would lead to 30 times higher ORR activity than pure Pt.[114] In the experiment, the 3ML-Pt/$Pt_{25}Ni_{75}$(111) alloy with −1.7% strain (close to the best strain of −0.2% in theoretical predictions) displayed enhanced activities for the ORR, consistent with the theoretical results.[83] For the FeCoPdIrPt system in the HER,[24] Fe, Co and Pd could downshift the d-band center of Pt, and more electrons could occupy the antibonding states, facilitating the desorption of hydrogen species to produce more hydrogen than the commercial Pt/C catalyst.

Considering that catalytic materials are usually nanoscale and the absolute magnitude of the induced strain is very small, strain along a certain direction is defined as $(l_f - l_i)/l_i$, where l_i and l_f represent the atomic bond length in the initial and final states, respectively.[105] It has been proven that the maximum catalytic activity required an optimum atomic bond length in catalysts.[115] A larger atomic bond length would cause oxygen dissociation before the adsorption in ORRs, whereas a smaller value would generate strong repulsive forces for dual-site adsorption.[115] Furthermore, an optimized surface strain can contribute to a high HER performance due to the small hydrogen adsorption Gibbs free energy on the catalytic sites.[116] Strain-induced changes in the atomic bond length can be viewed as the bulk lattice distortions in catalysts.[105] For HEAs, a serious lattice distortion effect gives rise to changes in the surface strain. The surface strain of HEAs can be tuned by selecting principal components with different atom radii. A seven-component FeNiCoSiCrAlTi HEA coating with BCC solid solution phase was prepared by laser cladding on a low carbon steel substrate.[117] The presence of the small-atomic-radius Si and large-atomic-radius Al and Ti increased the lattice packing density and crystal distortion. The segregation of Ti atom

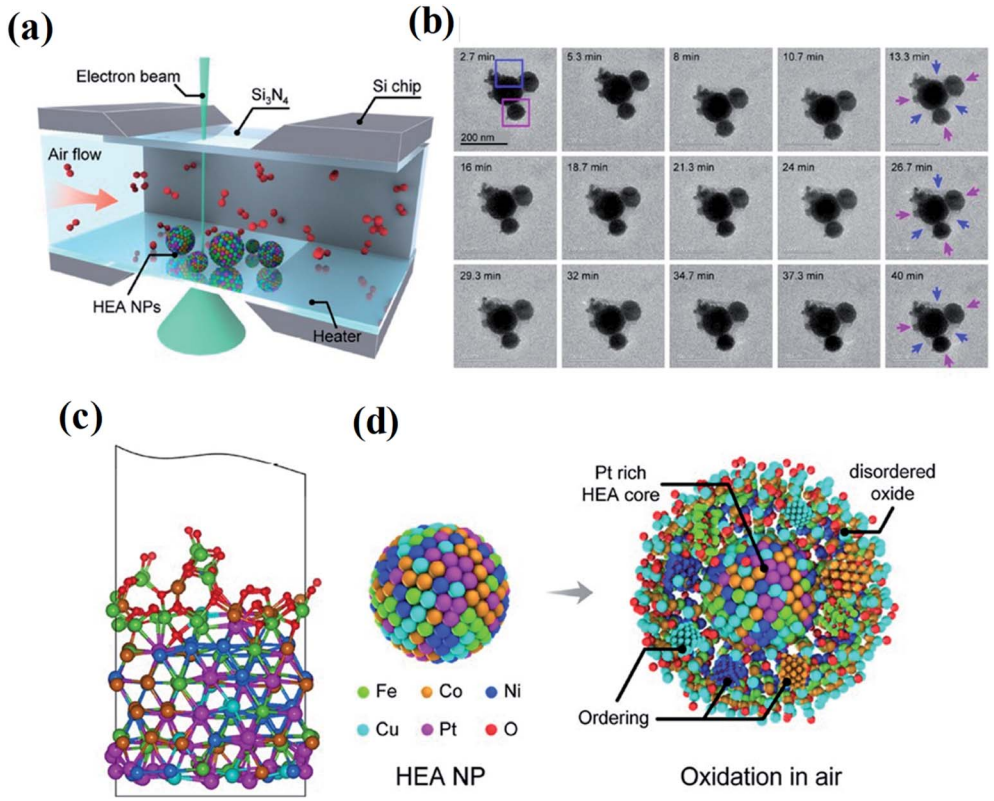

Fig. 22 (a) Schematic of the *in situ* gas-cell in air. (b) *In situ* TEM image sequences of HEA NPs during annealing in air to study the oxidation of HEA NPs. (c) Exemplary atomic model for an oxidized slab after equilibration. (d) Schematic illustration of the oxidation process of HEA NPs. Reproduced from ref. 152 with permission from the American Chemical Society.

caused the different lattice expansion and growth stress between Ti-depleted polygonal grains and Ti-enriched interdendrites, which can lead to increase of the contraction stress at their interfaces.[117] A higher concentration of Al, which has a larger atomic radius than Co, Ni, Fe, and Cu elements, resulted in a larger lattice distortion of $Co_{25}Ni_{25}Fe_{25}Al_{7.5}Cu_{17.5}$ with transformation of the HEA phase from FCC into a BCC structure.[118–120] This result revealed that the distribution of random elements with various atomic radii in HEAs can induce volume contraction or expansion along the specific direction. In addition, the local lattice distortion can result in the fluctuation of stacking fault (SF) energy.[121,122] The SF energy can change the number of SFs in catalysts, and thus tune their catalytic properties.[16] A high density of SFs in silver NPs caused a low coordination number and high tensile strain, transforming the non-active Ag into a highly active catalyst towards the HER.[116] The different atomic radii of the principal elements in HEAs can induce local strain effects due to the variation of SF energy.[34] SF–SF intersections produced a local strain field, leading to dislocation accumulation and SF formation in order to release the local strain concentration.[34] Based on the above mentioned analysis, it is expected that HEAs can optimize the surface strain, surface d-band width and SF density by selecting principal components with different atomic radii to achieve high catalytic activity.[123]

4.2.2 The ligand effect and d-band center. The ligand effect arises from the tuning of the surface electronic structure of the binding metal atom in a different atomic environment. It is affected by the surrounding metal atoms close to the binding site. Thus, this effect is considered to be short-range. The subtle shift of the d-band center can also be induced by the ligand effect. For example, when alloying non-noble metals such as Fe, Co, and Ni with Pt or Pd noble metals, the d electrons in the former tend to transfer to the latter, resulting in the d-band down-shift of noble metal atoms through the ligand effect due to the downshift of the Fermi level (Fig. 15).[124]

Owing to the ligand effect, the reactivity of one metal can be varied substantially by depositing it on another due to the adjustment of the d-band. Fig. 15b displays the d-band center change of a given metal when it is deposited on another metal, calculated by DFT.[125] This helps us to design HEAs with suitable components for a specific catalytic reaction. For instance, Pt is generally used as an anode catalyst for PEM fuel cells. However, the strong binding of CO on the Pt surface leads to poisoning of the catalyst. Finding a catalyst surface that weakly binds CO is desirable. As shown in Fig. 15b, a surface with weaker CO bonds than Pt(111) can be obtained by positioning Pt on top of atoms such as Ir, Rh, Ru, Cu, Fe, and Co, due to the down-shift of the Pt d-band.[125] Likewise, if a surface with stronger adsorption energy of intermediates is required, Pt can be put on atoms such as Ag or Au to up-shift the d-band center.

As lattice strain often changes the electronic structure of alloys, the strain effect and the ligand effect are difficult to be distinguished in practical HEA catalysts. To understand the contribution of the ligand effect, Rossmeisl *et al.* have isolated the electronic ligand effect of the HEA catalyst (IrPdPtRhRu) from the strain effect by creating an unstrained environment in DFT to investigate its ORR activity (Fig. 16).[126] After statistical analysis of 2000 DFT calculations and subsequent host/guest calculations, it has been found that selected atoms among the fourth nearest neighboring positions in the third layer of an FCC (111) metallic structure have more impact on the bond strength of an adsorbate in the ORR than any second or third nearest atomic positions.[126] It is found that the ligand effect affects both the d-band center and d-band shape which correlates closely with the bond strength of the adsorbate.

4.2.3 The ensemble effect. The ensemble effect, namely the geometric effect, refers to changes in the local chemisorption properties of an ensemble of atoms in the adsorption site when the ensemble composition changes. Compared with strain and ligand effects, the ensemble effect of alloys plays more significant roles in regulating the catalyst close to the reaction volcano peak,[127] because it can provide a well-tuned specific ensemble which binds adsorbates with an intermediate strength.

Alloys with distinct atomic ensembles result in different absorber binding strengths. When Au alloys with Pt as the catalyst in allyl alcohol hydrogenation, the H atoms are only adsorbed onto Pt sites.[127] Au atoms, which simply act as a surface diluent, have no impact on the H binding energy. PtAu catalysts exhibit a linear increase in activity with increasing Pt ratios.[127] However, when Pt atoms are replaced by Pd, H can interact with both Pd and Au atoms. Thus, the binding energy strength of H atoms on the Pd–Au atomic surface ensemble can be tuned to achieve improved hydrogenation activity. The contrasting behavior of PtAu and PdAu alloys is because different effects work in these two systems. The ensemble effect dominates the PtAu system, whereas PdAu alloys exhibit both ensemble and ligand effects. The ligand effect results in the direct charge transfer from Au to Pd atoms, leading to the d-band perturbation. These results provide valuable guidance for tuning the absorber binding energy by screening suitable components in HEAs.

Overall, the strain, ligand, ensemble effects and the d-band perturbation can significantly affect the adsorption energy of intermediates in catalytic reactions. The following section mainly discusses the relationship between the adsorption energy and catalytic activity of HEA catalysts.

4.3 Adsorption energy

A typical catalytic process usually involves the adsorption of reactants on catalysts, and chemical bond-breaking/formation between the catalyst and the reactants to generate activated intermediates.[128] The adsorption energy of the intermediates is the most important factor that determines the rate and selectivity of products in catalytic reactions because the catalytic activity is attributed to the interfacial electronic coupling.[128,129] According to the Sabatier principle, the measured activities as a function of the binding strength are plotted in a volcano curve.[94–96,130] It indicates that either too strong or too weak binding strength to the intermediates causes difficulty in removing the products or poor adsorption of the reactants, respectively.[97] The binding strength of catalysts is closely related to their structural properties. It is crucial to design catalysts with moderate binding strength.[131] Compared with the low intrinsic activity of the binary systems, which is related to the position of their elements in volcano plots, the HEA catalysts show enhanced activity due to the broad adsorption energy distribution easily covering favorable energies.[132] The cocktail effect of HEA catalysts can facilitate hybrid chemical and electronic interactions between metal components, thus affecting the adsorption energy of intermediates during catalytic reactions. For example, an alloying metal of $Ir_{0.19}Os_{0.22}Re_{0.21}Rh_{0.20}Ru_{0.19}$ with the HCP phase has been found to weaken the adsorption of CO in methanol oxidation due to the optimized electronic structures of the HEA catalyst, making CO easier to be removed.[55] The HEA alloy displayed higher yield and selectivity of CO in the methanol oxidation reaction than individual metals.[55] Schuhmann *et al.* discussed the effect of different adsorption energy distribution patterns on the activity curves of catalytic reactions by analyzing the experimental activity curves.[132] The number of adsorption peaks is the same as that of elements in HEAs. Each adsorption peak for HEAs contributes one exponentially increasing current curve of different activities governed by the position of the peak maximum regarding optimal binding energies.[132] Fig. 17a illustrates active site distribution within one adsorption peak. The model is simplified by reducing the number of active sites to 7. Active site 7 has the highest activity whereas active site 6 shows the least favorable binding energy.[132] In Fig. 17b, seven individual curves sum up to the overall measured curve, the activity of which is governed by the relative position of the respective peak maximum regarding optimal binding energies. To achieve high activity, a good fit of the best adsorption peak maximum with the optimal binding energy is required.[132] The position of the peaks in adsorption energy distribution patterns directly determines the shape of the catalytic curves. As shown in Fig. 17c, an overlap of the three most active peaks in the six-element CSS #6_2 causes difficult separation of all three wave segments in a catalytic curve.[132] In the case of the five-element CSS #5_2 with replaced elements, the third most active peak in the adsorption energy distribution pattern shifted towards unfavorable binding energies, resulting in only two wave segments within the considered regime. By comparison, the six-element CSS #6_1 shows the best peak.[132] Thus, the change in energy of the adsorption peaks on replacement or addition of elements is determined by the inherent properties of the material.

The optimization of adsorption energy has also been found when a nanocrystalline AuAgPtPdCu HEA was used for the electrocatalytic reduction of CO_2.[9] The faradaic efficiency is near 100% with respect to gaseous products at −0.3 V *vs.* reversible hydrogen electrode (RHE) due to a large number of catalytic sites present randomly on the surface of the HEA NPs, highlighting the uniqueness of the HEAs.[9] In CO_2 reduction, the conversion of $*OCH_3$ into the *O intermediate, which is an

endoergic reaction, has been considered the rate-determining step due to the high barrier. DFT calculation, based on the free-energy calculations of intermediates, demonstrated that the barrier is much lower for the HEA system (1.35 eV) than for the pristine Cu(111) (1.95 eV), as shown in Fig. 18.[9] The fact that the CO_2 reduction on the HEA NPs over the Cu(111) is thermodynamically favored should be attributed to the easier destabilization of $*OCH_3$ intermediates and the stronger stabilization of *O intermediates on the HEA surface than the Cu(111) surface. For stabilization of *O, both Pd[11] and Cu[7] atoms can bond O atoms on the HEA NP surface.[9] Notably, despite the presence of five elements in the HEA catalyst, the electrocatalytic activity is predominantly described by Cu atoms, and other atoms only provide a synergetic effect.[9]

Electrochemical HER is a classic two-electron-transfer reaction occurring through the Volmer–Heyrovsky mechanism. This mechanism involves two steps: Volmer step ($H^+ + e^- + * \rightarrow H^*$) and Heyrovsky step ($H^+ + e^- + H^* \rightarrow 0.5H_2 + *$). The corresponding free energy changes of the two steps are given by $\Delta G_{Volmer} = E_H{}^{ads} + \Delta E_{ZPE} - T\Delta S_H$ and $\Delta G_{Heyrovsky} = -E_H{}^{ads} - (\Delta E_{ZPE} - T\Delta S_H)$, where $E_H{}^{ads}$ is the hydrogen adsorption energy, ΔE_{ZPE} and ΔS_H are the difference in zero-point energy and the entropy difference between the adsorbed state and H_2, respectively.[133] Thus, $E_H{}^{ads}$ determines the overall HER activity. It has been found that the catalytic activity shows a volcano trend as a function of the hydrogen adsorption strength on catalyst sites (Fig. 19a).[134] The activity can be optimized when the adsorption energy of hydrogen species on catalysts is close to 0 V due to the balance of adsorption and desorption.[97] Although Pt is a high-activity catalyst for the HER, its scarcity limits its application. HEAs are expected to decrease the loading of noble metals without losing their electrocatalytic efficiencies as the cocktail effect can optimize the adsorption strength of hydrogen. In the FeCoPdIrPt system, the combination of Co with strong adsorption and Ir with weak adsorption can moderate the free energy of H species.[24] Pd, despite its poor HER activity, can modulate the hydrogen binding energy on the Pt surface.[97] Thus, the synergic effect of the atoms in the HEA NPs leads to excellent activity towards the HER.[24] In another work, an amorphous HEA of CoFeLaNiPt has also been found to show improved electrocatalytic performance compared to the individual components during the HER due to the elemental synergisms between Pt and other components on the atomic scale (Fig. 19b).[6]

The ORR in fuel cells usually involves four-proton–electron transfer to form H_2O.[135] During this process, the adsorption energy of intermediates such as O, OH and OOH on the surface of catalysts determines the catalytic activity of the ORR. The activity of metals with strong adsorption of the intermediates is limited by the proton transfer to the intermediates. For metals with weak adsorption of the intermediates, oxygen is unstable on the catalyst surface, thus no transfer of protons and electrons to oxygen occurs. A theoretical volcano-like trend between the activity and intermediate adsorption energy is also observed (Fig. 20a and b). Although Pt is near the top of the volcano-like trend, there still exists an overpotential of *ca.* 0.4 V for the ORR.[136,137] Pt-based alloys can reduce the overpotential by optimizing the intermediates' adsorption energy related to the pure Pt catalyst.[138,139] A first principles study has proven that transition metals can weaken the adsorption of chemical species to the Pt, leading to higher ORR activity.[140] Fig. 20c compares the calculated free energies of the steps in the ORR on CuNiPt and CuNiPtMn HEA surface systems.[79] The generation of the OOH* intermediate is the rate-limiting step of the ORR on both catalyst surfaces. Compared with CuNiPt, the addition of Mn in CuNiPtMn modulates the electronic properties of the catalyst surface, and thus optimizes the binding of OOH through the cocktail effect, resulting in enhanced activity (Fig. 20d and e).[79] The cocktail effect has also been found to be applicable to design advanced ORR catalysts without Pt, such as AlCuNiAgMn, AlCuNiAgMo, and AlCuNiAgCo, which even outperform the pure Pt catalyst.[79] The fact that the cocktail effect can optimize the adsorption energy of intermediates in the ORR is also proven by density functional theory (DFT), as shown in Fig. 21.[141] In order to achieve a highly efficient ORR reaction, *OH and *O intermediates must not be too stable on the surface of catalysts nor be easily removed. While Pt(111) is the best crystal surface of pure metal for the ORR, the adsorption energy of *OH (~0.1 eV) on it is still too strong.[136] According to the DFT results, the surface of an HEA catalyst can offer a near-continuous distribution of adsorption energy due to the complicated surface configurations.[141] Thus, a high-efficiency ORR can be achieved by tuning the compositions of the HEA catalyst with optimal adsorption energy close to the peak of the Sabatier volcano curve.[142] The HEA materials become a design platform for new alloys by increasing sites with superior catalytic activity to pure Pt(111).

5. Conclusions and perspectives

The emergence of HEA nanomaterials greatly promotes the development of non-noble-metal catalysts with high efficiency.[77,143–146] Due to the four core effects, HEAs can regulate the electronic and geometric structures to induce strain and d-band center shift, serving as a platform to construct catalysts with improved performance. However, the research of HEA catalysts is still in its early stage, and there still exist many issues that need to be addressed.

Firstly, scientific theories for the construction of HEAs is scarce. There are a huge number of possible compositions and combinations of properties in the HEA field. Wise element design strategies for suitable compositions and structures to fit the requirements in heterogeneous catalysis thus become especially important. The rational design of HEA nanomaterials from fundamental principles has the potential to create catalysts with high activity and selectivity.[147] Until now, designing new HEA materials is based on the traditional trial-and-error method which becomes very difficult due to the large number of possible compositions for HEAs. As the combinations of composition and process for producing HEAs are numerous, each HEA has its own microstructure and properties to be identified and understood. It is very important to present basic concepts relating to HEAs in advance. Using principles of materials science is the most basic way to design a new

material. This route can be used at the beginning to develop new HEA nanomaterials for desired properties by fully understanding the properties of components in materials, such as the crystal structure, atomic size, atomic weight, redox potential, electronegativity, melting and boiling points, density, electron configuration, *etc.* Rapid-throughput screening approaches are required to vet potential HEA compositions. For example, if we want to design low-density HEAs, more light elements should be used. If HEAs with oxidation resistance are needed, more oxidation-resistant elements such as Al, Cr, and Si should be selected. If HEAs with BCC phases are desired, Al can be added by strong binding with other elements to promote the formation of a BCC phase. In catalysis, Pd instead of Pt can be chosen as one of the components in HEAs to promote the catalytic activity due to the high electro-oxidation catalytic activity and lower price of Pd. In addition, both leverage neural network (NN) and machine learning can be employed to provide insights for rational design of HEA catalysts. The NN strategy can account for the three substitution effects of HEAs (mentioned in Fig. 13) for predicting the adsorption energy of catalysts.[148] Machine learning can help calculate adsorption energies of all surface sites on catalysts, allowing the optimization of the HEA compositions.[9,76] Nevertheless, there is also a risk that promising alloys might be dismissed in the early stage by these methods, due to the absence of exploration of the complex links between microstructures and properties. Certainly, careful experimental assessment of HEAs is the prerequisite to obtain the microstructure characteristics and stability.

Secondly, moderate and scalable synthesis strategies are urgently needed. Although current methods mentioned in Chapter 4 have successfully crafted HEA NPs, they generally require rigorous conditions such as high pressure, temperature and inert atmospheric protection. NPs can be only immobilized on limited thermally resistant substrates rather than thermally sensitive ones. It may incur great stoichiometric deviation due to the high vapor pressure of metal elements under these extreme conditions. The mild electrosynthesis method can only craft amorphous NPs (electrosynthesis method[6]) or is limited by the corresponding targets (PLA approach[44]). It is urgent to develop a more convenient technology with low energy consumption under mild conditions for synthesizing a library of HEA nanostructures.

Thirdly, although HEAs have shown great potential in catalysis applications, the understanding of the whole HEA world and how HEA materials behave in complex catalysis environments is still at the infant stage. Several future trends are pointed out: *more fundamental studies on HEA structures are required*. In most cases, the catalytic performance of HEA catalysts is simply explained by the synergetic effect between multiple elements. Very limited studies aim to establish an in-depth understanding of the structure–performance relationship. HEA structures with mutual interactions between different atoms, lattice distortion, metastable structures, stacking fault energy, electrical and thermal conductivity, diffusion coefficients, corrosion and oxidation are desired to fully understand the relationship between the structure and performance. Moreover, a theoretical model including microstructure details in HEAs will be instructive for establishing an accurate structure–performance relationship over HEA catalysts. Architectures in the atomic structures of HEAs can be explored in a systematic and site-specific manner. Otherwise, the possibility of comprehensively exploring such systems would be precluded. *Accurate models for catalyst selections need to be built*. The lack of such models makes the design of high-activity HEA catalysts difficult. The chosen descriptors determined the catalytic activities of catalysts. For example, the Sabatier principle shows a volcano-type relationship between catalytic activities and adsorption energy, whereas it is a linear relationship in the Brønsted–Evans–Polanyi behavior.[149,150] Due to the interactions of elements in alloys, the properties in terms of adsorption energy may be more complex. Establishing a descriptor suitable for HEA materials will contribute to guiding the selection of high-activity catalysts. *The behavior of HEA NPs in real service environments is investigated*. In the application of industrial catalysis, critical environments, such as high temperature/pressure, oxidizing/reducing conditions, and extreme pH solution, are usually involved.[151] Since it is challenging to obtain structural and compositional information of such nanoscale HEAs at spatial and temporal resolution, there is still very limited knowledge of the behavior of HEA NPs in these environments. Shahbazian-Yassar *et al.* employed *in situ* gas-cell TEM to investigate the oxidation behavior of $Fe_{0.28}Co_{0.21}Ni_{0.20}Cu_{0.08}Pt_{0.23}$ HEA NPs at 400 °C and in an atmospheric pressure air environment (Fig. 22).[152] Although the overall oxidation kinetics of the HEA NPs are slower than that of both monometallic and bimetallic alloy NPs with similar principal elements, the oxidation of HEA NPs governed by the Kirkendall effect has been found involving outward diffusion of Fe, Co, Ni, and Cu to form an oxide layer with a concentration gradient. Pt stays in the HEA core region during the oxidation process due to its nonreactivity. Studies on other extreme conditions such as oxidizing/reducing conditions and extreme pH solution are also needed, yet are still scarce, but are crucial for understanding HEA behavior in these environments and providing insights in designing chemical/thermal corrosion-resistant alloys for various applications.

Fourthly, more research can be focused on high-entropy ceramics (HECs) such as nitrides, carbides, oxides, and sulfides. A few studies have indicated that four core effects of HEAs are also applicable in HECs. As some conventional phosphides/sulfides/oxides/carbides/nitrides have been proven as efficient catalysts,[153–157] HECs are expected to have promising applications in catalysis *via* their four core effects. Unfortunately, there are few reports on the synthesis of HEC nanomaterials, limiting their research in the field of catalysis.

Based on these deliberations, HEAs have thrust us into a new world of seemingly infinite possibility. Research on HEA-based catalysis has been attracting increasing attention. Recent studies indeed offer significant potential to improve our fundamental understanding of the catalytic behavior of HEAs. Nevertheless, future efforts should focus on key features presented by the microstructures of HEAs, rather than wandering in its limitless expanse.

Conflicts of interest

There are no conflicts to declare.

Acknowledgements

This work was supported by the National Key Research and Development Program of China (2018YFE0208500), the Major Research Plan of the National Natural Science Foundation of China (91963206), the National Natural Science Foundation of China (52072169, 51627810, 51972164), the Natural Science Foundation of Jiangsu Province (BK20201202), the Program for Guangdong Introducing Innovative and Enterpreneurial Teams (2019ZT08L101), the Open Fund of Wuhan National Laboratory for Optoelectronics (2018WNLOKF020), Postgraduate Research & Practice Innovation Program of Jiangsu Province (KYCX19_0043), the Fundamental Research Funds for the Central Universities (14380193), and Civil Aerospace Technology Research Project (B0108).

References

1 Y. G. Yao, Z. Y. Liu, P. F. Xie, Z. N. Huang, T. Y. Li, D. Morris, Z. Finfrock, J. H. Zhou, M. L. Jiao, J. L. Gao, Y. M. Mao, J. W. Miao, P. Zhang, R. Shahbazian-Yassar, C. Wang, G. F. Wang and L. B. Hu, *Sci. Adv.*, 2020, **6**, eaaz0510.
2 X. Z. Wang, Q. Dong, H. Y. Qiao, Z. N. Huang, M. T. Saray, G. Zhong, Z. W. Lin, M. J. Cui, A. Brozena, M. Hong, Q. Q. Xia, J. L. Gao, G. Chen, R. Shahbazian-Yassar, D. W. Wang and L. B. Hu, *Adv. Mater.*, 2020, **32**, 2002853.
3 J. W. Yeh, S. K. Chen, S. J. Lin, J. Y. Gan, T. S. Chin, T. T. Shun, C. H. Tsau and S. Y. Chang, *Adv. Eng. Mater.*, 2004, **6**, 299–303.
4 D. B. Miracle and O. N. Senkov, *Acta Mater.*, 2017, **122**, 448–511.
5 Y. Zhang, Y. J. Zhou, J. P. Lin, G. L. Chen and P. K. Liaw, *Adv. Eng. Mater.*, 2008, **10**, 534–538.
6 M. W. Glasscott, A. D. Pendergast, S. Goines, A. R. Bishop, A. T. Hoang, C. Renault and J. E. Dick, *Nat. Commun.*, 2019, **10**, 2650.
7 P. F. Xie, Y. G. Yao, Z. N. Huang, Z. Y. Liu, J. L. Zhang, T. Y. Li, G. F. Wang, R. Shahbazian-Yassar, L. B. Hu and C. Wang, *Nat. Commun.*, 2019, **10**, 4011.
8 W. J. Dai, T. Lu and Y. Pan, *J. Power Sources*, 2019, **430**, 104–111.
9 S. Nellaiappan, N. K. Katiyar, R. Kumar, A. Parui, K. D. Malviya, K. G. Pradeep, A. K. Singh, S. Sharma, C. S. Tiwary and K. Biswas, *ACS Catal.*, 2020, **10**, 3658–3663.
10 S. Guo and C. T. Liu, *Prog. Nat. Sci.: Mater. Int.*, 2011, **21**, 433–446.
11 J. Chen, X. Y. Zhou, W. L. Wang, B. Liu, Y. K. Lv, D. P. Xu, W. Yang and Y. Liu, *J. Alloys Compd.*, 2019, **785**, 1294.
12 K. N. Zhao, X. Li and D. Su, *Acta Phys.-Chim. Sin.*, 2021, **37**, 2009077.
13 A. Amiri and R. Shahbazian-Yassar, *J. Mater. Chem. A*, 2021, **9**, 782–823.
14 X. H. Yan and Y. Zhang, *Scr. Mater.*, 2020, **187**, 188–193.
15 G. M. Tomboc, T. Kwon, J. Joo and K. Lee, *J. Mater. Chem. A*, 2020, **8**, 14844–14862.
16 B. Yaakobi, T. R. Boehly, D. D. Meyerhofer, T. J. B. Collins, B. A. Remington, P. G. Allen, S. M. Pollaine, H. E. Lorenzana and J. H. Eggert, *Phys. Rev. Lett.*, 2005, **95**, 075501.
17 Z. Y. Lv, X. J. Liu, B. Jia, H. Wang, Y. Wu and Z. P. Lu, *Sci. Rep.*, 2016, **6**, 34213.
18 Y. G. Yao, Z. N. Huang, P. F. Xie, S. D. Lacey, R. J. Jacob, H. Xie, F. J. Chen, A. M. Nie, T. C. Pu, M. Rehwoldt, D. W. Yu, M. R. Zachariah, C. Wang, R. Shahbazian-Yassar, J. Li and L. B. Hu, *Science*, 2018, **359**, 1489–1494.
19 S. Peulon and D. Lincot, *Adv. Mater.*, 1996, **8**, 166–170.
20 J. E. Dick, C. Renault, B. K. Kim and A. J. Bard, *Angew. Chem., Int. Ed.*, 2014, **53**, 11859–11862.
21 K. Huang, B. W. Zhang, J. S. Wu, T. Y. Zhang, D. D. Peng, X. Cao, Z. Zhang, Z. Li and Y. Z. Huang, *J. Mater. Chem. A*, 2020, **8**, 11938–11947.
22 A. Villa, D. Wang, D. S. Su and L. Prati, *Catal. Sci. Technol.*, 2015, **5**, 55–68.
23 E. D. Bojesen and B. B. Iversen, *Crystengcomm*, 2016, **18**, 8332–8353.
24 S. J. Gao, S. Y. Hao, Z. N. Huang, Y. F. Yuan, S. Han, L. C. Lei, X. W. Zhang, R. Shahbazian-Yassar and J. Lu, *Nat. Commun.*, 2020, **11**, 2016.
25 E. V. Shevchenko, D. V. Talapin, H. Schnablegger, A. Kornowski, O. Festin, P. Svedlindh, M. Haase and H. Weller, *J. Am. Chem. Soc.*, 2003, **125**, 9090–9101.
26 M. Bondesgaard, N. L. N. Broge, A. Mamakhel, M. Bremholm and B. B. Iversen, *Adv. Funct. Mater.*, 2019, **29**, 1905933.
27 C. J. Wang, X. R. Bao, G. W. Du, Y. Wang, K. Chen, M. L. Shen and L. Z. Wang, *Int. Urol. Nephrol.*, 2014, **46**, 1609–1617.
28 N. L. N. Broge, M. Bondesgaard, F. Sondergaard-Pedersen, M. Roelsgaard and B. B. Iversen, *Angew. Chem., Int. Ed.*, 2020, **59**, 21920–21924.
29 M. Y. Rekha, N. Mallik and C. Srivastava, *Sci. Rep.*, 2018, **8**, 8737.
30 S. H. Zhou, G. S. Jackson and B. Eichhorn, *Adv. Funct. Mater.*, 2007, **17**, 3099–3104.
31 S. Alayoglu and B. Eichhorn, *J. Am. Chem. Soc.*, 2008, **130**, 17479–17486.
32 M. M. Liu, Z. H. Zhang, F. Okejiri, S. Z. Yang, S. H. Zhou and S. Dai, *Adv. Mater. Interfaces*, 2019, **6**, 1900015.
33 Q. L. Li, H. L. Li, V. G. Pol, I. Bruckental, Y. Koltypin, J. Calderon-Moreno, I. Nowik and A. Gedanken, *New J. Chem.*, 2003, **27**, 1194–1199.
34 K. S. Suslick and G. J. Price, *Annu. Rev. Mater. Sci.*, 1999, **29**, 295–326.
35 S. H. Joo, J. W. Bae, W. Y. Park, Y. Shimada, T. Wada, H. S. Kim, A. Takeuchi, T. J. Konno, H. Kato and I. V. Okulov, *Adv. Mater.*, 2020, **32**, 1906160.
36 Z. Y. Jin, J. Lv, H. L. Jia, W. H. Liu, H. L. Li, Z. H. Chen, X. Lin, G. Q. Xie, X. J. Liu, S. H. Sun and H. J. Qiu, *Small*, 2019, **15**, 1904180.
37 C. X. Xu, R. Y. Wang, Y. Zhang and Y. Ding, *Nanoscale*, 2010, **2**, 906–909.

38 H. J. Qiu, G. Fang, Y. R. Wen, P. Liu, G. Q. Xie, X. J. Liu and S. H. Sun, *J. Mater. Chem. A*, 2019, **7**, 6499–6506.
39 M. M. Biener, J. Biener, A. Wichmann, A. Wittstock, T. F. Baumann, M. Baumer and A. V. Hamza, *Nano Lett.*, 2011, **11**, 3085–3090.
40 C. F. Tsai, P. W. Wu, P. Lin, C. G. Chao and K. Y. Yeh, *Jpn. J. Appl. Phys.*, 2008, **47**, 5755–5761.
41 G. W. Yang, *Prog. Mater. Sci.*, 2007, **52**, 648–698.
42 A. V. Kabashin and M. Meunier, *J. Appl. Phys.*, 2003, **94**, 7941–7943.
43 V. Amendola, S. Scaramuzza, F. Carraro and E. Cattaruzza, *J. Colloid Interface Sci.*, 2017, **489**, 18–27.
44 F. Waag, Y. Li, A. R. Ziefuss, E. Bertin, M. Kamp, V. Duppel, G. Marzun, L. Kienle, S. Barcikowski and B. Gokce, *RSC Adv.*, 2019, **9**, 18547–18558.
45 P. Wagener, A. Schwenke, B. N. Chichkov and S. Barcikowski, *J. Phys. Chem. C*, 2010, **114**, 7618–7625.
46 E. P. George, D. Raabe and R. O. Ritchie, *Nat. Rev. Mater.*, 2019, **4**, 515–534.
47 H. Q. Song, F. Y. Tian, Q. M. Hu, L. Vitos, Y. D. Wang, J. Shen and N. X. Chen, *Phys. Rev. Mater.*, 2017, **1**, 023404.
48 B. Fultz, *Prog. Mater. Sci.*, 2010, **55**, 247–352.
49 J. W. Yeh, *JOM*, 2013, **65**, 1759–1771.
50 J. W. Yeh, *Ann. Chimie Sci. Matériaux*, 2006, **31**, 633–648.
51 F. Y. Tian, *Front. Mater.*, 2017, **4**, 36.
52 B. Cantor, I. T. H. Chang, P. Knight and A. J. B. Vincent, *Mater. Sci. Eng., A*, 2004, **375**, 213–218.
53 Y. Pei, G. B. Zhou, N. Luan, B. N. Zong, M. H. Qiao and F. Tao, *Chem. Soc. Rev.*, 2012, **41**, 8140–8162.
54 J. F. Deng, H. X. Li and W. J. Wang, *Catal. Today*, 1999, **51**, 113–125.
55 K. V. Yusenko, S. Riva, P. A. Carvalho, M. V. Yusenko, S. Arnaboldi, A. S. Sukhikh, M. Hanfland and S. A. Gromilov, *Scr. Mater.*, 2017, **138**, 22–27.
56 P. F. Xie, Y. G. Yao, Z. N. Huang, Z. Y. Liu, J. L. Zhang, T. Y. Li, G. F. Wang, R. Shahbazian-Yassar, L. B. Hu and C. Wang, *Nat. Commun.*, 2019, **10**, 4011.
57 M. H. Tsai and J. W. Yeh, *Mater. Res. Lett.*, 2014, **2**, 107–123.
58 Y. F. Kao, T. J. Chen, S. K. Chen and J. W. Yeh, *J. Alloys Compd.*, 2009, **488**, 57–64.
59 S. Ranganathan, *Curr. Sci.*, 2003, **85**, 1404–1406.
60 Y. J. Zhou, Y. Zhang, Y. L. Wang and G. L. Chen, *Appl. Phys. Lett.*, 2007, **90**, 181904.
61 S. Singh, N. Wanderka, B. S. Murty, U. Glatzel and J. Banhart, *Acta Mater.*, 2011, **59**, 182–190.
62 K. Zhao, X. X. Xia, H. Y. Bai, D. Q. Zhao and W. H. Wang, *Appl. Phys. Lett.*, 2011, **98**, 141913.
63 R. N. Singh, A. Singh and Anindita, *Int. J. Hydrogen Energy*, 2009, **34**, 2052–2057.
64 Z. Qi, H. R. Geng, X. G. Wang, C. C. Zhao, H. Ji, C. Zhang, J. L. Xu and Z. H. Zhang, *J. Power Sources*, 2011, **196**, 5823–5828.
65 S. Kasatikov, A. Fantin, A. M. Manzoni, S. Sakhonenkov, A. Makarova, D. Smirnov, E. O. Filatova and G. Schumacher, *J. Alloys Compd.*, 2021, **857**, 157597.
66 G. L. Zhang, K. S. Ming, J. L. Kang, Q. Huang, Z. J. Zhang, X. R. Zheng and X. F. Bi, *Electrochim. Acta*, 2018, **279**, 19–23.
67 K. Y. Tsai, M. H. Tsai and J. W. Yeh, *Acta Mater.*, 2013, **61**, 4887–4897.
68 Q. F. He and Y. Yang, *Front. Mater.*, 2018, **5**, 42.
69 K. Chen, S. Kim, R. Rajendiran, K. Prabakar, G. Z. Li, Z. C. Shi, C. Y. Jeong, J. Kang and O. L. Li, *J. Colloid Interface Sci.*, 2021, **582**, 977–990.
70 C. F. Tsai, K. Y. Yeh, P. W. Wu, Y. F. Hsieh and P. Lin, *J. Alloys Compd.*, 2009, **478**, 868–871.
71 A. L. Wang, H. C. Wan, H. Xu, Y. X. Tong and G. R. Li, *Electrochim. Acta*, 2014, **127**, 448–453.
72 J. Barranco and A. R. Pierna, *J. Non-Cryst. Solids*, 2008, **354**, 5153–5155.
73 X. T. Chen, C. H. Si, Y. L. Gao, J. Frenzel, J. Z. Sun, G. Eggeler and Z. H. Zhang, *J. Power Sources*, 2015, **273**, 324–332.
74 Z. Y. Lv, X. J. Liu, B. Jia, H. Wang, Y. Wu and Z. P. Lu, *Sci. Rep.*, 2016, **6**, 34213.
75 S. K. Wu, Y. Pan, N. Wang, T. Lu and W. J. Dai, *Int. J. Miner., Metall. Mater.*, 2019, **26**, 124–132.
76 D. S. Wu, K. Kusada, T. Yamamoto, T. Toriyama, S. Matsumura, I. Gueye, O. Seo, J. Kim, S. Hiroi, O. Sakata, S. Kawaguchi, Y. Kubota and H. Kitagawa, *Chem. Sci.*, 2020, **11**, 12731–12736.
77 C. S. Zhou, R. C. Bowman, Z. Z. Fang, J. Lu, L. Xu, P. Sun, H. Liu, H. Wu and Y. Liu, *ACS Appl. Mater. Interfaces*, 2019, **11**, 38868–38879.
78 M. M. Shi, D. Bao, S. J. Li, B. R. Wulan, J. M. Yan and Q. Jiang, *Adv. Energy Mater.*, 2018, **8**, 1800124.
79 S. Y. Li, X. W. Tang, H. L. Jia, H. L. Li, G. Q. Xie, X. J. Liu, X. Lin and H. J. Qiu, *J. Catal.*, 2020, **383**, 164–171.
80 Y. G. Yao, Z. N. Huang, T. Y. Li, H. Wang, Y. F. Liu, H. S. Stein, Y. M. Mao, J. L. Gao, M. L. Jiao, Q. Dong, J. Q. Dai, P. F. Xie, H. Xie, S. D. Lacey, I. Takeuchi, J. M. Gregoire, R. Z. Jiang, C. Wang, A. D. Taylor, R. Shahbazian-Yassar and L. B. Hu, *Proc. Natl. Acad. Sci. U. S. A.*, 2020, **117**, 6316–6322.
81 S. A. Kube and J. Schroers, *Scr. Mater.*, 2020, **186**, 392–400.
82 C. J. H. Jacobsen, S. Dahl, B. S. Clausen, S. Bahn, A. Logadottir and J. K. Norskov, *J. Am. Chem. Soc.*, 2001, **123**, 8404–8405.
83 P. M. Forster, J. Eckert, B. D. Heiken, J. B. Parise, J. W. Yoon, S. H. Jhung, J. S. Chang and A. K. Cheetham, *J. Am. Chem. Soc.*, 2006, **128**, 16846–16850.
84 K. S. Suslick, S. B. Choe, A. A. Cichowlas and M. W. Grinstaff, *Nature*, 1991, **353**, 414–416.
85 H. Zahn and J. Kramer, *Z. Phys.*, 1933, **86**, 413–420.
86 H. I. Schlesinger, H. C. Brown, A. E. Finholt, J. R. Gilbreath, H. R. Hoekstra and E. K. Hyde, *J. Am. Chem. Soc.*, 1953, **75**, 215–219.
87 J. Vanwonterghem, S. Morup, C. J. W. Koch, S. W. Charles and S. Wells, *Nature*, 1986, **322**, 622–623.
88 Z. Li, J. Y. Fu, Y. Feng, C. K. Dong, H. Liu and X. W. Du, *Nat. Catal.*, 2019, **2**, 1107–1114.
89 A. Molnar, G. V. Smith and M. Bartok, *Adv. Catal.*, 1989, **36**, 329–383.
90 H. Li, K. Shin and G. Henkelman, *J. Chem. Phys.*, 2018, **149**, 174705.

91 J. W. Yeh, S. K. Chen, J. Y. Gan, S. J. Lin, T. S. Chin, T. T. Shun, C. H. Tsau and S. Y. Chang, *Metall. Mater. Trans. A*, 2004, **35a**, 2533–2536.
92 D. F. Wu, J. C. Zhou and Y. D. Li, *AIChE J.*, 2007, **53**, 2618–2629.
93 D. F. Wu, L. Y. Song, B. Q. Zhang and Y. D. Li, *Chem. Eng. Sci.*, 2003, **58**, 3995–4004.
94 V. Stamenkovic, B. S. Mun, K. J. J. Mayrhofer, P. N. Ross, N. M. Markovic, J. Rossmeisl, J. Greeley and J. K. Norskov, *Angew. Chem., Int. Ed.*, 2006, **45**, 2897–2901.
95 A. J. Medford, A. Vojvodic, J. S. Hummelshoj, J. Voss, F. Abild-Pedersen, F. Studt, T. Bligaard, A. Nilsson and J. K. Norskov, *J. Catal.*, 2015, **328**, 36–42.
96 F. Abild-Pedersen, J. Greeley, F. Studt, J. Rossmeisl, T. R. Munter, P. G. Moses, E. Skulason, T. Bligaard and J. K. Norskov, *Phys. Rev. Lett.*, 2007, **99**, 016105.
97 W. C. Sheng, M. Myint, J. G. G. Chen and Y. S. Yan, *Energy Environ. Sci.*, 2013, **6**, 1509–1512.
98 D. Voiry, H. Yamaguchi, J. W. Li, R. Silva, D. C. B. Alves, T. Fujita, M. W. Chen, T. Asefa, V. B. Shenoy, G. Eda and M. Chhowalla, *Nat. Mater.*, 2013, **12**, 850–855.
99 M. Mavrikakis, B. Hammer and J. K. Norskov, *Phys. Rev. Lett.*, 1998, **81**, 2819–2822.
100 J. R. Kitchin, J. K. Norskov, M. A. Barteau and J. G. Chen, *Phys. Rev. Lett.*, 2004, **93**, 156801.
101 J. Hwang, R. R. Rao, L. Giordano, Y. Katayama, Y. Yu and Y. Shao-Horn, *Science*, 2017, **358**, 751–756.
102 X. L. Tian, X. Zhao, Y. Q. Su, L. J. Wang, H. M. Wang, D. Dang, B. Chi, H. F. Liu, E. J. M. Hensen, X. W. Lou and B. Y. Xia, *Science*, 2019, **366**, 850–856.
103 B. Hammer and J. K. Norskov, *Surf. Sci.*, 1995, **343**, 211–220.
104 L. A. Kibler, A. M. El-Aziz, R. Hoyer and D. M. Kolb, *Angew. Chem., Int. Ed.*, 2005, **44**, 2080–2084.
105 M. C. Luo and S. J. Guo, *Nat. Rev. Mater.*, 2017, **2**, 17059.
106 S. Schnur and A. Gross, *Phys. Rev. B: Condens. Matter Mater. Phys.*, 2010, **81**, 033402.
107 K. Yan, T. A. Maark, A. Khorshidi, V. A. Sethuraman, A. A. Peterson and P. R. Guduru, *Angew. Chem., Int. Ed.*, 2016, **55**, 6175–6181.
108 H. T. Wang, S. C. Xu, C. Tsai, Y. Z. Li, C. Liu, J. Zhao, Y. Y. Liu, H. Y. Yuan, F. Abild-Pedersen, F. B. Prinz, J. K. Norskov and Y. Cui, *Science*, 2016, **354**, 1031–1036.
109 L. Wang, Z. H. Zeng, W. P. Gao, T. Maxson, D. Raciti, M. Giroux, X. Q. Pan, C. Wang and J. Greeley, *Science*, 2019, **363**, 870–874.
110 M. Escudero-Escribano, P. Malacrida, M. H. Hansen, U. G. Vej-Hansen, A. Velazquez-Palenzuela, V. Tripkovic, J. Schiotz, J. Rossmeisl, I. E. L. Stephens and I. Chorkendorff, *Science*, 2016, **352**, 73–76.
111 P. Strasser, S. Koh, T. Anniyev, J. Greeley, K. More, C. F. Yu, Z. C. Liu, S. Kaya, D. Nordlund, H. Ogasawara, M. F. Toney and A. Nilsson, *Nat. Chem.*, 2010, **2**, 454–460.
112 M. Asano, R. Kawamura, R. Sasakawa, N. Todoroki and T. Wadayama, *ACS Catal.*, 2016, **6**, 5285–5289.
113 N. Todoroki, Y. Iijima, R. Takahashi, Y. Asakimori and T. Wadayama, *J. Electrochem. Soc.*, 2013, **160**, F591–F596.
114 I. E. L. Stephens, A. S. Bondarenko, U. Gronbjerg, J. Rossmeisl and I. Chorkendorff, *Energy Environ. Sci.*, 2012, **5**, 6744–6762.
115 V. Jalan and E. J. Taylor, *J. Electrochem. Soc.*, 1983, **130**, 2299–2301.
116 Z. Li, J. Y. Fu, Y. Feng, C. K. Dong, H. Liu and X. W. Du, *Nat. Catal.*, 2019, **2**, 1107–1114.
117 H. Zhang, Y. Pan, Y. Z. He and H. S. Jiao, *Appl. Surf. Sci.*, 2011, **257**, 2259–2263.
118 J. Li, Q. H. Fang, B. Liu and Y. Liu, *Acta Mater.*, 2018, **147**, 35–41.
119 Z. Q. Fu, W. P. Chen, H. M. Wen, D. L. Zhang, Z. Chen, B. L. Zheng, Y. Z. Zhou and E. J. Lavernia, *Acta Mater.*, 2016, **107**, 59–71.
120 B. Gludovatz, A. Hohenwarter, K. V. S. Thurston, H. B. Bei, Z. G. Wu, E. P. George and R. O. Ritchie, *Nat. Commun.*, 2016, **7**, 10602.
121 S. Y. Liu and Y. J. Wei, *Extreme Mechanics Letters*, 2017, **11**, 84–88.
122 A. J. Zaddach, C. Niu, C. C. Koch and D. L. Irving, *JOM*, 2013, **65**, 1780–1789.
123 M. Kim, C. Lee, S. M. Ko and J. M. Nam, *J. Solid State Chem.*, 2019, **270**, 295–303.
124 K. Jiang, H. X. Zhang, S. Z. Zou and W. B. Cai, *Phys. Chem. Chem. Phys.*, 2014, **16**, 20360–20376.
125 T. Bligaard and J. K. Norskov, *Electrochim. Acta*, 2007, **52**, 5512–5516.
126 C. M. Clausen, T. A. A. Batchelor, J. K. Pedersen and J. Rossmeisl, *Adv. Sci.*, 2021, **8**, 2003357.
127 L. Luo, Z. Y. Duan, H. Li, J. Kim, G. Henkelman and R. M. Crooks, *J. Am. Chem. Soc.*, 2017, **139**, 5538–5546.
128 Y. W. Wang, W. J. Qiu, E. H. Song, F. Gu, Z. H. Zheng, X. L. Zhao, Y. Q. Zhao, J. J. Liu and W. Q. Zhang, *Natl. Sci. Rev.*, 2018, **5**, 327–341.
129 C. T. Campbell, *Acc. Chem. Res.*, 2019, **52**, 984–993.
130 F. Z. Song, W. Li and Y. J. Sun, *Inorganics*, 2017, **5**, 40.
131 F. Z. Song, W. Li, J. Q. Yang, G. Q. Han, T. Yan, X. Liu, Y. Rao, P. L. Liao, Z. Cao and Y. J. Sun, *ACS Energy Lett.*, 2019, **4**, 1594–1601.
132 T. Loffler, A. Savan, H. Meyer, M. Meischein, V. Strotkotter, A. Ludwig and W. Schuhmann, *Angew. Chem., Int. Ed.*, 2020, **59**, 5844–5850.
133 J. K. Norskov, T. Bligaard, A. Logadottir, J. R. Kitchin, J. G. Chen, S. Pandelov and J. K. Norskov, *J. Electrochem. Soc.*, 2005, **152**, J23–J26.
134 J. D. Benck, T. R. Hellstern, J. Kibsgaard, P. Chakthranont and T. F. Jaramillo, *ACS Catal.*, 2014, **4**, 3957–3971.
135 W. Li, D. H. Xiong, X. F. Gao and L. F. Liu, *Chem. Commun.*, 2019, **55**, 8744–8763.
136 J. K. Norskov, J. Rossmeisl, A. Logadottir, L. Lindqvist, J. R. Kitchin, T. Bligaard and H. Jonsson, *J. Phys. Chem. B*, 2004, **108**, 17886–17892.
137 V. Viswanathan, H. A. Hansen, J. Rossmeisl and J. K. Norskov, *ACS Catal.*, 2012, **2**, 1654–1660.
138 V. R. Stamenkovic, B. S. Mun, M. Arenz, K. J. J. Mayrhofer, C. A. Lucas, G. F. Wang, P. N. Ross and N. M. Markovic, *Nat. Mater.*, 2007, **6**, 241–247.

139 J. Greeley, I. E. L. Stephens, A. S. Bondarenko, T. P. Johansson, H. A. Hansen, T. F. Jaramillo, J. Rossmeisl, I. Chorkendorff and J. K. Norskov, *Nat. Chem.*, 2009, **1**, 552–556.
140 Z. Y. Duan and G. F. Wang, *Phys. Chem. Chem. Phys.*, 2011, **13**, 20178–20187.
141 T. A. A. Batchelor, J. K. Pedersen, S. H. Winther, I. E. Castelli, K. W. Jacobsen and J. Rossmeisl, *Joule*, 2019, **3**, 834–845.
142 K. D. Jensen, J. Tymoczko, J. Rossmeisl, A. S. Bandarenka, I. Chorkendorff, M. Escudero-Escribano and I. E. L. Stephens, *Angew. Chem., Int. Ed.*, 2018, **57**, 2800–2805.
143 K. D. Gilroy, A. Ruditskiy, H. C. Peng, D. Qin and Y. N. Xia, *Chem. Rev.*, 2016, **116**, 10414–10472.
144 M. K. Debe, *Nature*, 2012, **486**, 43–51.
145 H. A. Gasteiger and N. M. Markovic, *Science*, 2009, **324**, 48–49.
146 I. E. L. Stephens, J. Rossmeisl and I. Chorkendorff, *Science*, 2016, **354**, 1378–1379.
147 J. K. Pedersen, T. A. A. Batchelor, D. X. Yan, L. E. J. Skjegstad and J. Rossmeisl, *Curr. Opin. Electrochem.*, 2021, **26**, 100651.
148 Z. L. Lu, Z. W. Chen and C. V. Singh, *Matter*, 2020, **3**, 1318–1333.
149 A. Logadottir, T. H. Rod, J. K. Norskov, B. Hammer, S. Dahl and C. J. H. Jacobsen, *J. Catal.*, 2001, **197**, 229–231.
150 T. Bligaard, J. K. Norskov, S. Dahl, J. Matthiesen, C. H. Christensen and J. Sehested, *J. Catal.*, 2004, **224**, 206–217.
151 Y. Z. Shi, B. Yang and P. K. Liaw, *Metals*, 2017, **7**, 43.
152 B. Song, Y. Yang, M. Rabbani, T. T. Yang, K. He, X. B. Hu, Y. F. Yuan, P. Ghildiyal, V. P. Dravid, M. R. Zachariah, W. A. Saidi, Y. Z. Liu and R. Shahbazian-Yassar, *ACS Nano*, 2020, **14**, 15131–15143.
153 C. F. Wise and J. M. Mayer, *J. Am. Chem. Soc.*, 2020, **142**, 12544–12545.
154 H. M. Sun, Z. H. Yan, F. M. Liu, W. C. Xu, F. Y. Cheng and J. Chen, *Adv. Mater.*, 2020, **32**, 1806326.
155 Y. L. Zhu, Q. Lin, Y. J. Zhong, H. A. Tahini, Z. P. Shao and H. T. Wang, *Energy Environ. Sci.*, 2020, **13**, 3361–3392.
156 T. X. Nguyen, Y. H. Su, C. C. Lin, J. Ruan and J. M. Ting, *Adv. Sci.*, 2021, **8**, 2002446.
157 H. Chen, Y. F. Sun, S. Z. Yang, H. Wang, W. Dmowski, T. Egami and S. Dai, *Chem. Commun.*, 2020, **56**, 15056–15059.

